STRONG AND WEAK LIGHT-MATTER INTERACTIONS IN PLASMONIC AND OPTICAL CAVITIES

A Thesis Submitted to
the Graduate School of Engineering and Sciences of
İzmir Institute of Technology
in Partial Fulfillment of the Requirements for the Degree of

DOCTOR OF PHILOSOPHY

in Photonics

by
Nahit Polat

December 2023

İZMİR

We approve the thesis of **Nahit POLAT**

Examining Committee Members:

Prof. Dr. Sinan Balcı
Department of Photonics, IYTE

Assoc. Prof. Dr. Özgür Çakır
Department of Physics, IYTE

Assoc. Prof. Dr. Ü.Hakan Yıldız
Department of Chemistry, IYTE

Asst. Prof. Dr. Murat Alkan
Department of Metallurgy and Materials Engineering, DEU

Assoc. Prof. Dr. Muhammed Üçüncü
Department of Pharmacy, İKÇU

11 December 2023

Prof.Dr. Sinan Balcı
Supervisor, Department of Photonics
IYTE

Prof. Mustafa Emrullahoğlu
Co-Supervisor, Department of
Photonics IYTE

Prof. Dr. Canan Varlıklı
Head of the Department of
Photonics

Prof. Dr. Mehtap EANES
Dean of the Graduate School of
Engineering and Sciences

ACKNOWLEDGMENTS

I would like to express my deepest gratitude to Prof. Dr. Sinan BALCI for his guidance and continuous support throughout my PhD journey. His constant help, insightful suggestions and unlimited patience were truly instrumental in the successful completion of this thesis. It was an honor and a pleasure to have the privilege to learn and grow under his supervision. I am eternally grateful for his invaluable contribution to my academic and personal development.

I would like to thank my committee members of my thesis Assoc. Prof. Dr. Özgür ÇAKIR, Assoc. Prof. Dr. Ü. Hakan YILDIZ, Assoc. Prof. Dr. Muhammed ÜÇÜNCÜ, and Assist. Prof. Dr. Murat ALKAN for their participations. I am also thankful to Assist. Prof. Dr. Fadime MERT BALCI for her motivation and great contributions to this thesis.

To my dear lab friends especially Sema SARISÖZEN, Meriç GÜVENÇ, Ayhan TERTEMİZ, Tuğçe ARICA GÜVENÇ who never hesitate to share their friendship, their help whenever I need it, their time, who allow me to spend a unique time sometimes in academic life and sometimes in social life, and for their contribution to me in overcoming every problem during this time; I would like to thank everyone.

ABSTRACT

STRONG AND WEAK LIGHT-MATTER INTERACTIONS IN PLASMONIC AND OPTICAL CAVITIES

This thesis investigates the interaction of light and matter through both experimental and theoretical approaches, focusing on two key topics: Strong and Weak coupling.

We also examine the field of strong light-matter interactions under two headings: plasmonic and optical cavities. In the section on plasmonic cavities, we focus on the strong coupling between surface plasmon polaritons and excitons with different optical properties and localized surface plasmon resonance. We also discuss the strong coupling between localized surface plasmon resonance and excitons in plasmonic nanoparticles with different optical properties due to their different shapes. This thesis focuses on the theoretical and optical characterization of the aforementioned topics. Therefore, details on the manufacturing processes are not given. Instead, it presents a comparative analysis of optical measurement results and related simulation data, to which I have contributed more. In addition, we demonstrate for the first time hyperspectral imaging of exciton polaritons at optical microcavities. Two metal thin films acting as reflectors and a polymer matrix containing a collection of quantum emitters form the hybrid system for polariton imaging. We show a strong exciton-photon interaction between photons trapped in the microcavity and Frenkel excitons of dye molecules placed inside the optical microcavity. We find that exciton polaritons in the optical microcavity can be imaged and spatially mapped using hyperspectral imaging in the visible region.

In the field of weak light-matter interactions, the focus of the thesis is on the Fano resonance, which is a unique case in the weak coupling regime. The degree of coupling between interacting systems plays a critical role in determining the extent to which constructive and destructive interference phenomena occur in the system. An important example of destructive interference is the Fano resonance, which is caused by interference between two optical paths that are characterized by different states: one is narrow and discrete, and the other is broad and continuum. This is the first study to theoretically investigate the destructive interference between subwavelength excitonic nanoparticles

placed on the surface of a prism for Fano resonance observations and the evanescent wave scattering on the prism surface. In an attempt to understand the intricate dynamics between the evanescent wave and the Fano resonance, we study the effect of changing the angle of incidence of the incident plane wave on the properties of the Fano resonance. Furthermore, we also investigate how the size of the excitonic nanoparticles and the absorption linewidth influence the properties of the Fano resonance.

ÖZET

PLAZMONİK VE OPTİK KAVİTELERDE GÜÇLÜ VE ZAYIF IŞIK MADDE ETKİLEŞİMLERİ

Bu tez, ışık ve maddenin etkileşimini hem deneysel hem de teorik yaklaşımlarla araştırmakta ve iki temel konuya odaklanmaktadır: Güçlü ve Zayıf etkileşme. Güçlü ışık-madde etkileşimleri alanını da iki başlık altında inceliyoruz: Plazmonik ve Optik Boşluklar. Plazmonik kaviteler bölümünde, yüzey plazmon polaritonları ile farklı optik özelliklere sahip eksitonlar ve lokalize yüzey plazmon rezonansı arasındaki güçlü eşleşmeye odaklanıyoruz. Ayrıca, farklı şekilleri nedeniyle farklı optik özelliklere sahip plazmonik nanoparçacıklardaki yerelleştirilmiş yüzey plazmon rezonansı ile eksitonlar arasındaki güçlü etkileşmeyi de tartışıyoruz. Bu tez, yukarıda bahsi geçen konuların teorik ve optik karakterizasyonuna odaklanmaktadır. Bu nedenle, üretim süreçleriyle ilgili ayrıntılar verilmemiştir. Bunun yerine, çalışma optik ölçüm sonuçlarının ve ilgili simülasyon verilerinin karşılaştırmalı bir analizini sunmaktadır. Bunun yerine, daha çok katkımın bulunduğu optik ölçüm sonuçlarının ve ilgili simülasyon verilerinin karşılaştırmalı bir analizini sunmaktadır. Buna ek olarak, optik mikrokavitelerde eksiton polaritonların hiperspektral görüntülemesini ilk kez gösteriyoruz. Yansıtıcı görevi gören iki metal ince film ve bir kuantum yayıcı koleksiyonu içeren bir polimer matris, polariton görüntüleme için hibrit sistemi oluşturuyor. Mikro boşlukta hapsolmuş fotonlar ile optik mikro boşluk içine yerleştirilmiş boya moleküllerinin Frenkel eksitonları arasında güçlü bir eksiton-foton etkileşimi olduğunu gösteriyoruz. Optik mikro boşluktaki eksiton polaritonlarının görünür bölgede hiperspektral görüntüleme kullanılarak görüntülenebileceğini ve uzamsal olarak haritalanabileceğini bulduk.

Zayıf ışık-madde etkileşimleri alanında, tezin odak noktası zayıf bağlaşım rejiminde benzersiz bir durum olan Fano rezonansıdır. Etkileşen sistemler arasındaki bağlantı derecesi, sistemde yapıcı ve yıkıcı girişim olaylarının ne ölçüde meydana geldiğinin belirlenmesinde kritik bir rol oynar. Yıkıcı girişimin önemli bir örneği, farklı durumlarla karakterize edilen iki optik yol arasındaki girişimin neden olduğu Fano rezonansıdır: biri dar ve ayrık, diğeri geniş ve süreklidir. Bu çalışma, Fano rezonans gözlemleri için bir prizmanın yüzeyine yerleştirilen alt dalga boylu eksitonik

nanoparçacıklar ile prizma yüzeyindeki evanesant dalga saçılımı arasındaki yıkıcı girişimi teorik olarak araştıran ilk çalışmadır. Evanesant dalga ve Fano rezonansı arasındaki karmaşık dinamikleri anlamak amacıyla, gelen düzlem dalganın geliş açısını değiştirmenin Fano rezonansının özellikleri üzerindeki etkisini inceliyoruz. Ayrıca, eksitonik nanoparçacıkların boyutunun ve soğurma çizgi genişliğinin Fano rezonansının özelliklerini nasıl etkilediğini de araştırıyoruz.

to my family…

TABLE OF CONTENTS

LIST OF FIGURES

CHAPTER 1

INTRODUCTION

This chapter covers the basic building blocks of the light-matter interaction used in this thesis. This chapter describes the strong and weak coupling regimes studied throughout the thesis, the optical structures and nanoparticles used to form these couplings, the experimental setups used for the measurements, and the simulation methodology employed.

1.1 Fundamentals of Light-Matter Interactions

We perceive the world in different shapes and colors due to the complex effects of light-matter interactions. Scientific efforts to understand the fundamental principles governing these interactions have enabled answers to questions about a variety of visual phenomena. For example: Why can we enjoy daylight on Earth, while space remains in darkness despite the constant presence of the Sun? Why do some materials either reflect, absorb, or transmit light? Why do objects that are under water appear to be bent or closer to the outside observer? Our understanding of the interaction of light and matter, including scattering, transmission, refraction, and dispersion, has answered these questions and more, and increased our knowledge of the observable world around us (Hecht, 2012).

The fundamental optical processes that govern the interactions between light and matter are the sequential absorption and emission of photons by the absorbing medium. When a photon of energy $h\omega_1$ strikes a material (figure 1.1), photons can be absorbed by the material if it has a transition of the same or higher energy, and photons of energy $h\omega_2$ can be emitted if there is a suitable band structure (figure 1.1). Furthermore, a diverse range of light-matter interactions can arise, contingent upon the characteristics of the incident light field (frequency, polarization, and intensity), the nature of the material (size, chemical composition, electronic density, etc.), and the prevailing conditions of the interaction (medium, phase relations, angle of incidence, etc.).

In principle, we can define the light-matter interaction regime under two headings: weak and strong coupling regimes. The coupling strength changes the future of the photon

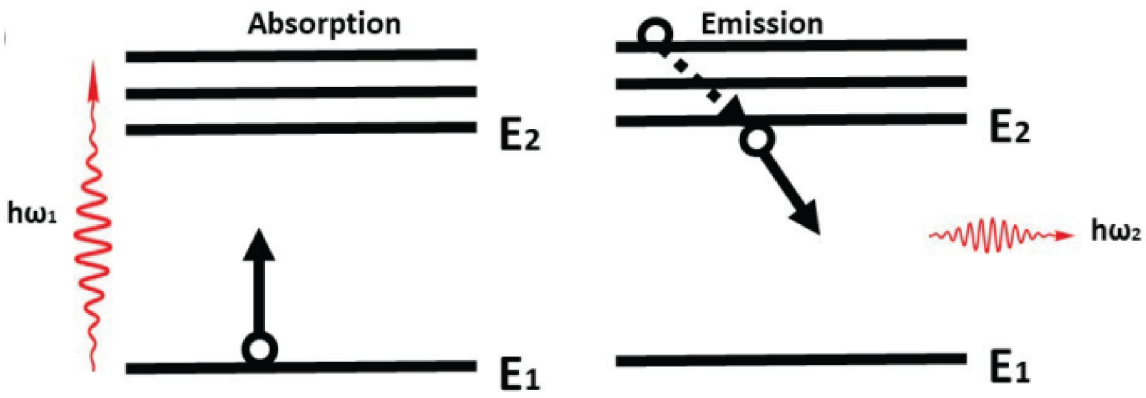

Figure 1.1. Schematic illustration of the absorption and emission

after the absorption/emission process. In the case of weak coupling, the emitted photon escapes the system and causes a negligible interaction with matter. As a result, the photon and matter can have destructive and constructive effects on each other (Miroshnichenko et al., 2010), while they are expected to remain separate and independently measurable entities. Under conditions that allow continuous interaction between the photon and the matter, characterized by multiple absorption and emission cycles, the system transitions to the strong coupling regime. This regime is characterized by the interaction of the photon and the matter, resulting in novel hybrid light-matter eigenstates (Lidzey et al., 2000).

1.1.1 Coupling Regimes

A pair of harmonic oscillators with energy exchange capability can be effectively modelled as a single coupled oscillator system (figure 1.2). Two coupled mechanical oscillators can exchange energy through a spring of coupling strength κ, with energy losses due to external forces. The behaviour of the coupled system is strongly driven by the interplay between the energy exchange and dissipation mechanisms that determine the transition from the weak to the strong coupling regime. The critical point at which the rate of energy exchange exceeds the rate of energy dissipation marks the onset of the coupling regime. Similarly, the energy exchange between light and matter is governed by the coupling factor, which determines the strength of the interaction.

$\gamma_{1,2}$ in figure 1.3, which are dissipative losses for oscillators. As noted earlier, the degree of coupling in the system can be characterized as weak or strong regimes by manipulating the associated losses. A critical aspect of this process is the precise positioning of the coupling strength between the oscillators relative to the dissipative losses of the system. The coupling strength, which is determined by the energy exchange

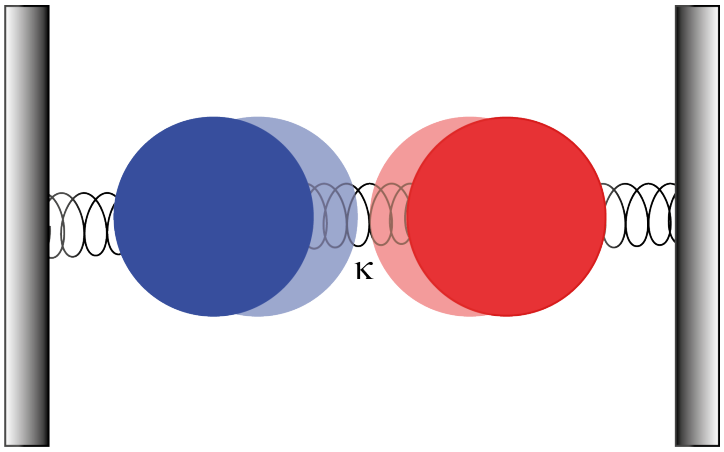

Figure 1.2. Schematic illustration of two coupled oscillator

between the oscillators ($\gamma_{1,2}$) and the coupling strength parameter (g). If $\gamma_{1,2} < g$ the oscillators are strongly coupled and have a significant mutual influence. Conversely, when $\gamma_1 \ll g$ or $\gamma_2 \ll g$ the coupling is considered weak and the oscillators show minimal interaction (Limonov et al., 2017). The red shaded regions in Figure 1.3 describe a special case of weak coupling and will be discussed in detail in Chapter 3.

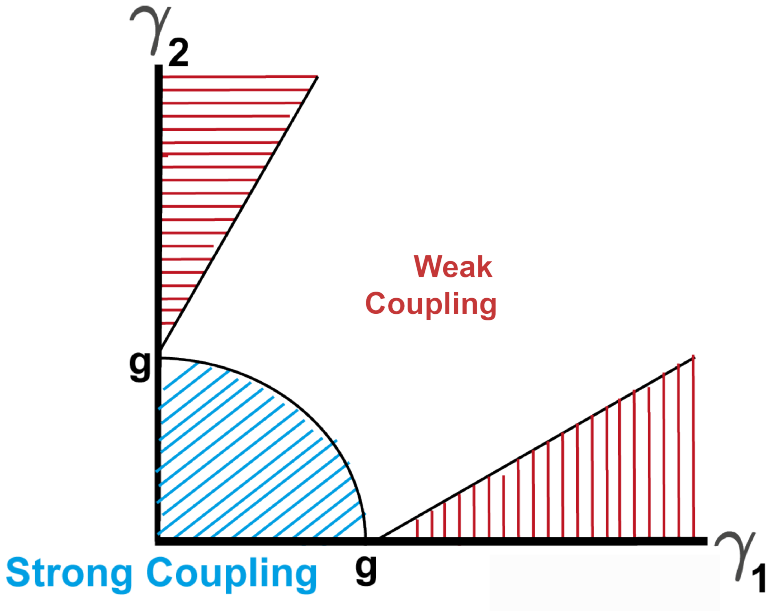

Figure 1.3. Schematic illustration of weak coupling and strong coupling limits.

1.1.1.1 The Strong Coupling Regimes

As shown in figure 1.4, under suitable conditions, energy exchange between absorbing and resonating light modes can occur. When the energy exchange rate exceeds all dissipation processes during the interaction ($\gamma_{1,2} < g$), a strong coupling is established. Specifically, dissipation can occur by radiative decay or by relaxation of the excited state (Rodriguez, 2016). Under the above conditions, the strong coupling leads to the formation of two new hybrid light-matter states, called polaritonic states. These polaritonic states arise from the hybridization of photonic and matter-based excitations, e.g. between cavity photons and excitons, and between plasmon and exciton resonance couplings. This complex light-matter interaction leads to the formation of different polaritonic modes, each characterized by a unique energy distribution and mixing ratio of photonic and matter-based excitation components. The characteristic of hybrid states is Rabi splitting, which is closely related to the transition energy dipole moment of the material, the number of particles used, and the intensity of the specifically designed electric field.

When strong light-matter coupling involves the interaction of many molecules with an optical mode, the hybrid states are delocalized over many molecules and the Rabi splitting is enhanced, affecting the properties of the coupled system (Balci et al., 2019). Strong light-matter coupling can be achieved with various optical systems. In this thesis, we will focus on the strong coupling regimes produced by resonant surface plasmon polariton (SPP) modes and localized surface plasmon resonance (LSPR) modes of plasmonic nanoparticles, as well as resonant Fabry-Perot (FP) cavity modes (in Chapter 2).

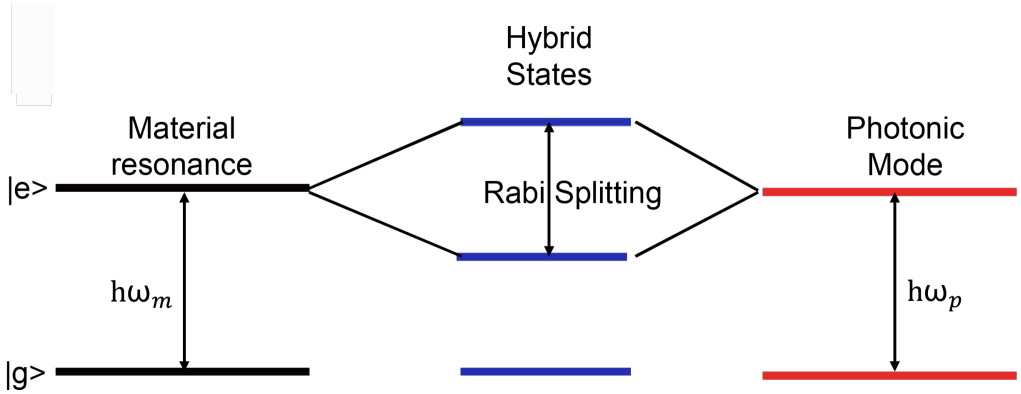

Figure 1.4. Schematic representation of the strong coupling regime.

1.1.1.2 The Weak Coupling Regimes

Under conditions of weak light-matter interaction, loss processes reduce the efficient energy transfer between photons and matter. Under conditions of weak light-matter interaction, loss processes affect the efficient energy transfer between photons and matter, so that destructive and constructive interference can occur between the electric fields generated by light and matter. Moving from the classical model to an absorber embedded in a cavity, a qualitatively similar behavior between the light fields emerges in both configurations. The radiation rate of the matter can be modified by the interaction, but there can be some phase shifts and changes in the Lorentz shape of the spectrum, although there is no obvious change in the emission frequency of the molecule (Limonov et al., 2017). In this case, there is destructive interference between light and matter (Miroshnichenko et al., 2010). The interference between a dipole resonance and the electric field generated by the interaction of gold nanoparticles with light leads to a dipole decay rate that increases with decreasing distance (figure 1.5), thus ultimately enhance the dipole resonance (Ozceri et al., 2021). This is called constructive interference (Miroshnichenko et al., 2010).

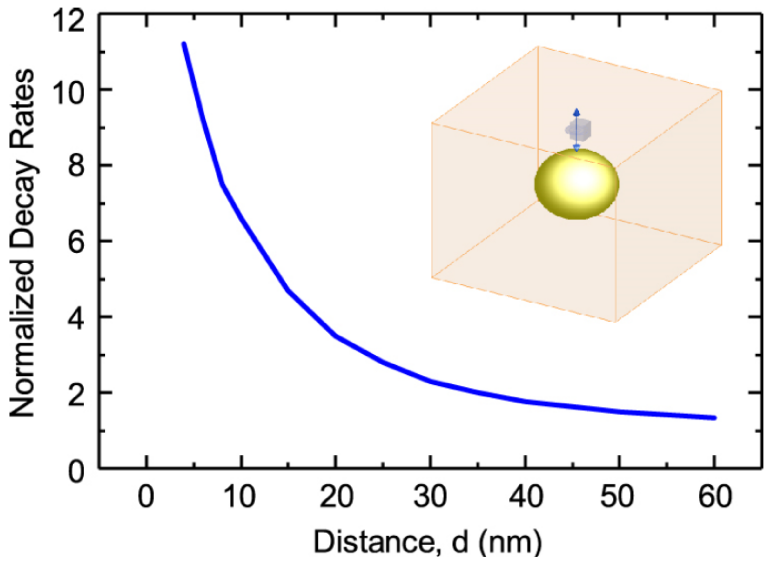

Figure 1.5. Calculation of non-radiative decay rates from a dipole position to gold

The weak coupling regime will be discussed in more detail in Chapter 3. Experimental and theoretical studies on constructive and destructive interference will also be presented.

1.2 Matters Used in Light Matter Interaction

This section explores the fundamental ingredients that facilitate the emergence of both strong and weak coupling regimes and examines their results in detail in later chapters. In doing so, the fundamental elements governing interparticle interactions will be examined. This comprehensive analysis will provide a fundamental framework for understanding the various functions and potential applications associated with these different binding regimes.

1.2.1 Plasmonic Cavities

This chapter explores the fundamental surface plasmon polariton (SPP) and localized surface plasmon resonance (LSPR) phenomena that underlie strong light-matter interactions.

1.2.1.1 Surface Plasmons Polariton

At the interface between a dielectric and a metal, solutions to Maxwell's equations for electromagnetic waves, known as surface plasmon polaritons (SPPs), exist. These solutions, called eigenmodes, can be described independently of any incident field.

Considering a planar interface between dielectric and metallic half-spaces with permittivities ε_d and ε_d, respectively, surface plasmon polaritons (SPPs) are TM-polarized plane waves propagating along the interface. Assuming a normal $\hat{z}$ oriented interface and SPP propagation along the x-axis ($k_y = 0$), the SPP wave vector k_x is related to the optical frequency ω via the dispersion relation (Raether, 2006)

$$k_x = k_0 \sqrt{\frac{\varepsilon_d \varepsilon_m}{\epsilon_d + \epsilon_m}}, \tag{1.1}$$

where $k_0 = \frac{\omega}{c}$ is free space wave-vector. Stationary monochromatic SPP fields are generated in a finite field by restricting our approach to real ω and complex k_x (Archambault et al., 2009).

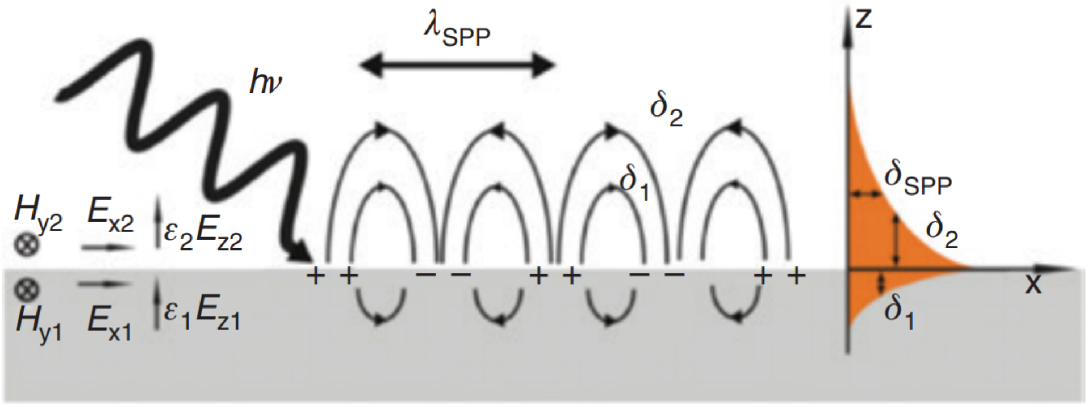

Figure 1.6. Schematic illustration of surface plasmon polaritons (Safiabadi Tali and Zhou, 2019).

The established Drude model, which describes the behaviour of a free electron gas, is often used to analyse the optical response of metals (Kittel, 2005),

$$\varepsilon_{Drude}(\omega) = 1 - \frac{\omega_p^2}{\omega^2 + i\Gamma\omega} \tag{1.2}$$

where ω_p is the plasma frequency, Γ represents the total attenuation rate due to both electron-electron and electron-phonon scattering mechanisms.

In figure 1.7, the dispersion curve (Eq.1.2) for a Drude metal-air. When the permittivity of the metal ε_m is less than the negative of the permittivity of air ($-\varepsilon_d$), which implies frequencies below the surface plasmon resonance frequency $\omega_{sp} = \omega_p\sqrt{1+\varepsilon_d}$, the SPP wave vector exceeds k_0, placing the dispersion curve to the right of the light line. As a result, the field decreases exponentially perpendicular to the interface due to the evanescent wave relationship between k_z and k_x. The large real component k_x of the wave vector corresponds to an important transverse (vertical) constraint, which is directly governed by the imaginary component k_z. Figure 1.7 shows a typical z dependence of the SPP H_y field.

For all frequencies ω, the wave vector $k_x = k_x^{'} + ik_x^{''}$ becomes complex due to inherent losses. In figure 1.7. the imaginary component of the wave vector ($k_x^{''}$) is plotted, which represents the magnitude of the propagation losses along the x-direction. Figure 1.7 shows a rapid increase in loss as the frequency approaches ω_{sp}. This is due to the increasing transverse confinement of the SPP mode, which results in a larger fraction of the modal field residing within the metal and consequently increased ohmic dissipation. This dissipation limits the efficiency of light concentration in nanoscale volumes using SPPs. The trade-off between the advantageous properties of SPPs and ohmic losses is a critical challenge for many practical applications of plasmonics. Among metals, silver

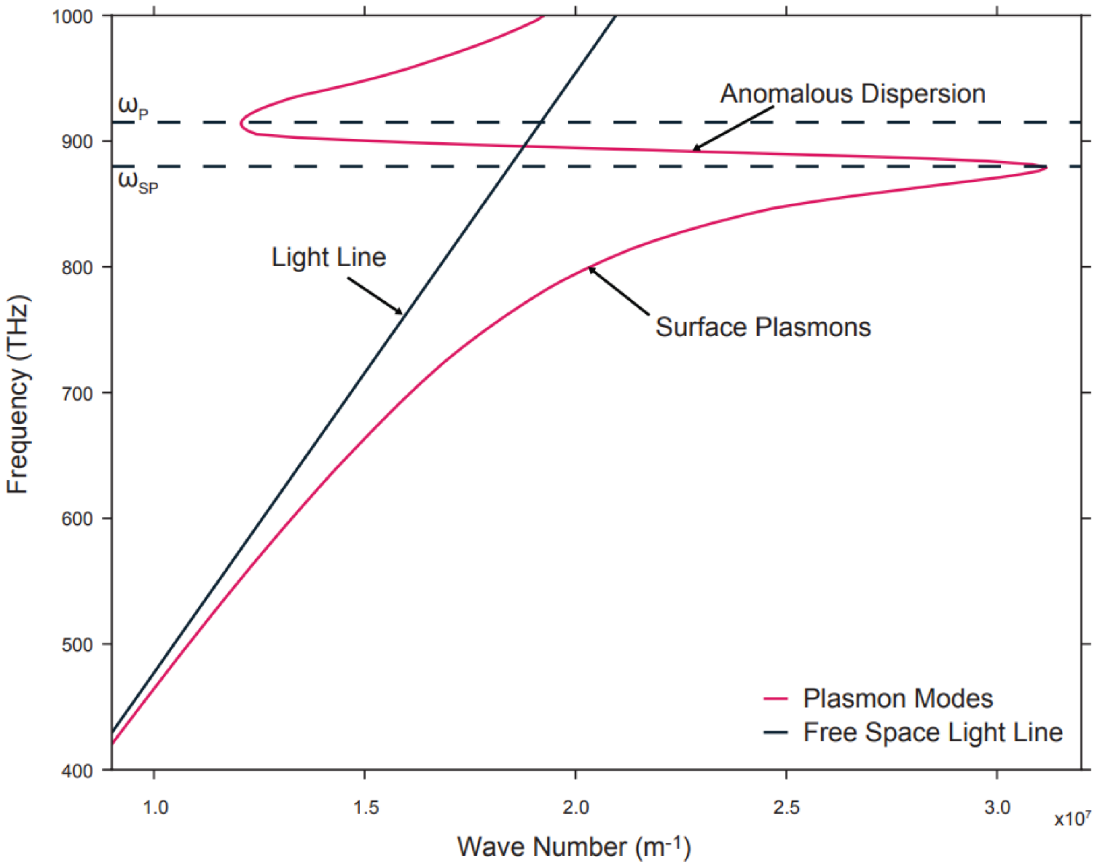

Figure 1.7. Dispersion curve of SPP.

(Ag) exhibits the lowest absorption while maintaining a large negative real part of ε_m over the visible and near-infrared spectrum. Gold (Au) serves as a viable alternative for the near-infrared region.The metal Ag was used in the studies in Chapter 2 because of its ability to mediate strong light-matter interactions via surface plasmon polaritons (SPPs) in the visible spectrum, the resonant region of the absorbers used in this thesis.

1.2.1.2 Localized Surface Plasmons Resonance

Excitation of localized surface plasmon resonances (LSPRs) in metallic nanoparticles creates localized oscillations of the electron density, resulting in the trapping and guiding of light along the nanoparticle surface at wavelengths that coincide with an absorption-like resonance (figure 1.8).

Upon interaction with incident photons, localized surface plasmon resonance (LSPR) is excited in metal nanoparticles. LSPRs arise from the interaction between the electric field of the incident light and the free electrons of the nanoparticle, leading to the formation of a collective dipole oscillation. Consequently, only light with a fre-

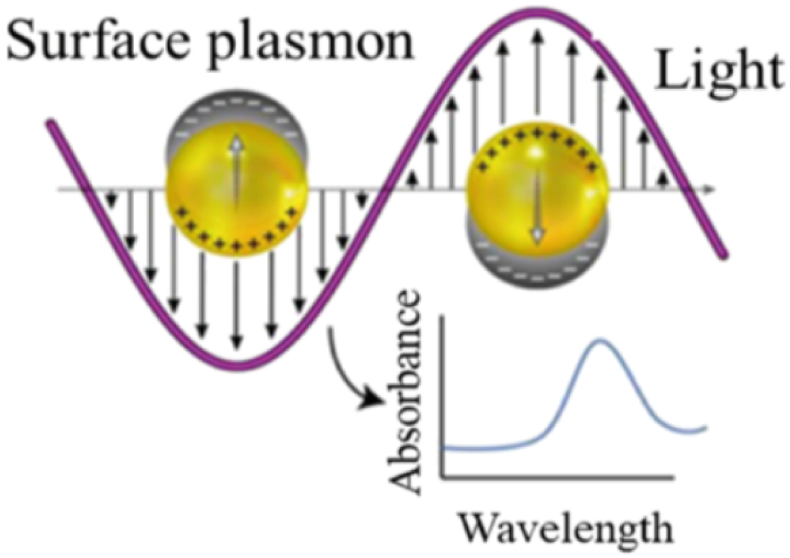

Figure 1.8. Schematic representation of LSPR in a spherical metal nanoparticle (Indhu et al., 2023).

quency matching the resonant frequency of the free electron oscillation is absorbed by the nanoparticle.

LSPR in metal nanoparticles shows a strong dependence on the morphology of the nanoparticles themselves, including their size and shape, as well as on the refractive index of the surrounding medium (Pala et al., 2009). The variable resonance resulting from both size and shape variations can provide a strong coupling, allowing specific interaction with an absorber. In this thesis, the creation of a strong coupling regime using silver nanodiscs, nanorods, and pentagonal bimetallic nanoparticles composed of silver and gold is investigated and the related results are presented in Chapter 2.

1.2.2 Optical Microcavities

Optical microcavities formed by planar Fabry-Perot configurations with highly reflective mirrors provide a powerful platform to study the interaction between light and matter in the context of cavity quantum electrodynamics (CQED). Successive reflections within the microcavity generate standing waves and trap photons in a small volume, enabling light-matter interactions. The dynamics of these systems are governed by fundamental parameters: emitter-cavity coupling strength (g), which measures the interaction between the emitter and the cavity mode, and cavity decay rate (κ) and non-resonant emitter decay rate (γ), which determine the rate of photon emission from the system. In addition, the non-resonant emitter decay rate (γ) exerts a significant influence on the

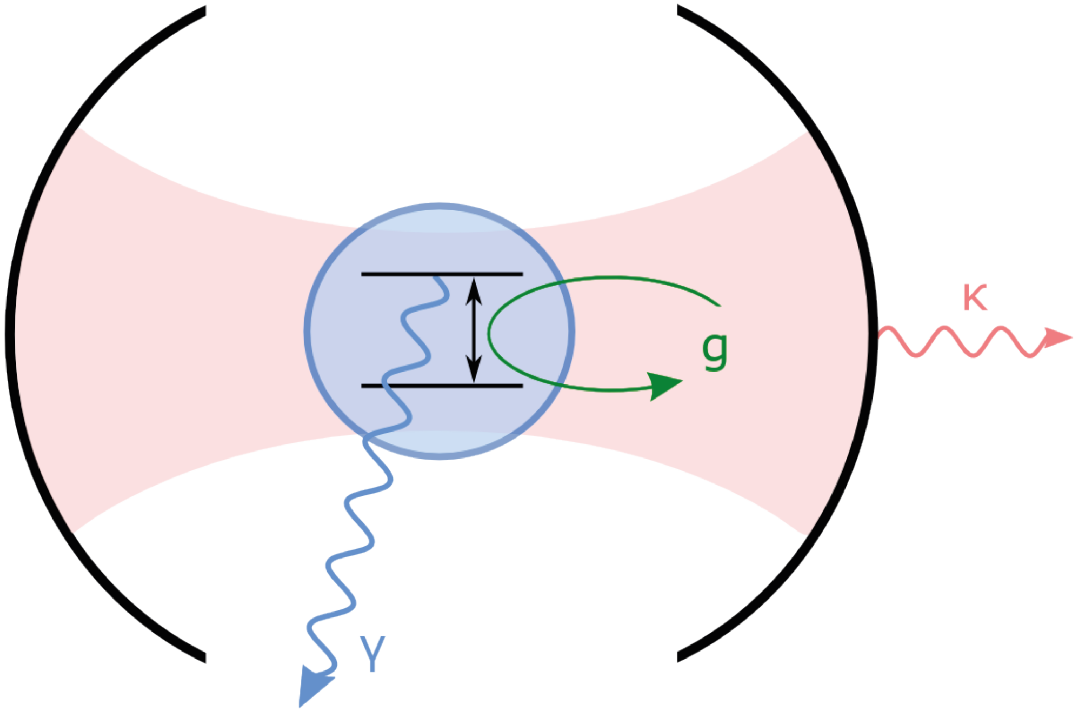

Figure 1.9. Basic representation of cavity

overall system dynamics. The relative magnitudes of γ, the cavity field decay rate (κ), and the system coupling strength (g) determine the dominant physical regime within the microcavity. Each regime exhibits unique properties and provides valuable insights into the fundamental principles of cavity quantum electrodynamics (CQED). In the weak coupling regime, the dissipative losses significantly exceed the strength of the emitter-cavity interaction ($\kappa, \gamma \gg \Omega_{Rabi}/2$). In this regime, the cavity modifies the local density of optical states, resulting in either enhancement or suppression of the emission rate, a phenomenon known as the Purcell effect. In the strong coupling limit, characterized by a Rabi frequency (Ω_{Rabi}) exceeding both the cavity decay rate (κ) and the emitter dephasing rate (γ), the emitted energy is reabsorbed before it can escape from the cavity ($\kappa, \gamma \ll \Omega_{Rabi}/2$). This leads to the establishment of a cyclic energy exchange between the emitter and the cavity, known as a Rabi cycle. This cyclic interaction leads to a characteristic energy splitting, which signifies the emergence of novel quasiparticles known as polaritons. These hybrid entities possess properties of both light and matter, existing as half-light, half-matter composites.

The cavity resonant wavelength (λ_c) is determined by the cavity spacing and can be expressed as:

$$\lambda_c = \frac{2n_{eff}L_{eff}}{m} \tag{1.3}$$

where n_{eff} is the effective cavity refractive index, L_{eff} is effective length of the cavity, m is the longitudinal mode index, chosen to closely match the resonance of the active region within the cavity.

This thesis presents a comprehensive analysis of the strong coupling regime facilitated by strategically matching optical cavities according to their first longitudinal mode index, as will be detailed in Chapter 2.

1.2.3 Excitons

A quasiparticle found in a wide variety of materials, including insulators, semiconductors, selected metals, and even some atoms, molecules, and liquids, an exciton is formed when an electron is excited from a lower energy state to a higher energy state, leaving a vacancy (hole). Attracted by the Coulomb force, the electron and hole can remain bound for a finite time, forming an exciton.

The generation of excitons in semiconducting materials requires the excitation by photons with an energy that exceeds the band gap energy of the material. When excited by photons that cross their band gaps, semiconductors or insulators undergo electron promotion to the conduction band by absorbed photon energy, leaving behind positively charged holes. This coulombically bound electron-hole pair, called an exciton, is electrically neutral. The concept of excitons was first introduced by Yakov Frenkel in 1931 (Frenkel, 1931).

Excitons, quasiparticles resulting from the bound state of an electron and a hole, exhibit different properties depending on the strength of their internal electron-hole interactions. This interaction energy determines the spatial localization and mobility of the exciton and leads to two different classifications: Frenkel and Wannier-Mott excitons.

Frenkel excitons are elementary excitations in organic semiconductors characterized by a strong Coulomb interaction between the excited electron and the remaining hole, resulting from a low dielectric constant environment. This strong interaction results in a tightly bound exciton state with a small exciton Bohr radius, typically on the order of a few nanometers (Liang, 1970). The binding energy of Frenkel excitons is substantial, ranging from 0.1 to 1.0 eV (Kéna-Cohen and Forrest, 2010), and contributes significantly to their stability.

Organic semiconductors are a natural habitat for Frenkel excitons due to their inherently low dielectric constants and strong intermolecular interactions. In particular, J-aggregate dyes represent a particularly well-studied and widely used class of organic materials that exhibit prominent Frenkel exciton behavior (figure 1.10(b)). Their

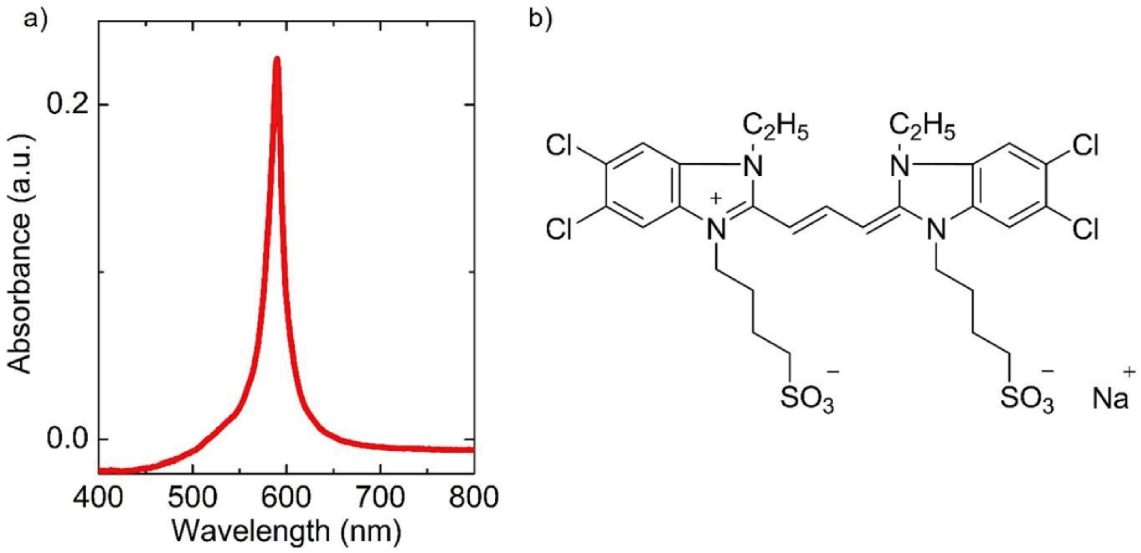

Figure 1.10. As a TDBC J-aggregate dye in this work, a cyanine dye

unique molecular structure and spatial arrangement facilitate efficient exciton transport and light-harvesting capabilities, making them valuable for various applications in organic electronics and photovoltaics.

Wannier-Mott excitons are neutral quasiparticles consisting of an excited bound state electron and its associated Coulomb hole in a high dielectric constant solid (Wannier, 1937). They can move along the lattice without carrying a net charge. The exciton radius of a Wannier-Mott exciton is a few lattice constants and its binding energy is as low as 0.01 eV (Kéna-Cohen and Forrest, 2010). This makes it more "delocalized" than a Frenkel exciton. These excitons are typically found in high dielectric constant semiconductors where the electric field gap reduces the Coulomb interaction between particles. The radius of a Wannier-Mott exciton is significantly larger than the lattice spacing.

In this thesis, exciton sources J-aggregate dyes and carbon quantum dots (CDs) are used for strong and weak ligth matter interaction.

1.3 Background of Experimental Set-ups

This section discusses the basic principles and objectives of the experimental configurations implemented to study the samples generated in the strong coupling regime.

1.3.1 Absorption and Emission Spectroscopy

The experimental setup was specifically designed and used to obtain the absorption spectra of the exciton sources used in this thesis, the extinction spectra of silver nanoparticles, and the extinction spectra of plexitonic nanoparticles as a result of the strong coupling regime. All measurements were carefully performed at room temperature in solvents suitable for exciton sources to ensure controlled and consistent conditions for accurate data collection. This rigorous approach minimized potential artifacts and facilitated subsequent analysis and interpretation of the acquired spectra.

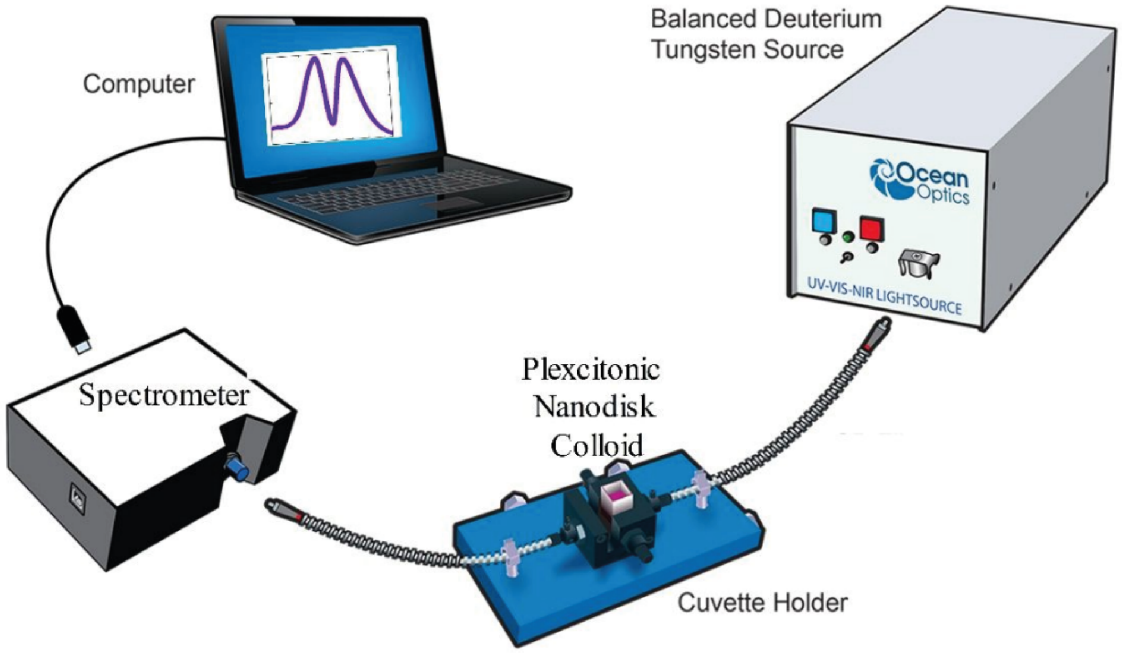

Figure 1.11. Schematic representation of Uv-vis spectrophotometer.

The absorption spectra of the colloidal samples were characterized using a basic optical setup. A deuterium-tungsten light source was used to study the optical properties of the sample. This broad spectrum source provided the necessary illumination for both absorption and transmission measurements, allowing data to be collected over a wide wavelength range. A force holder facilitated efficient coupling and transmission of light through optical fibers, allowing precise spectral measurements with a high-resolution spectrometer(Ocean Optics).

1.3.2 Kretschmann Configuration

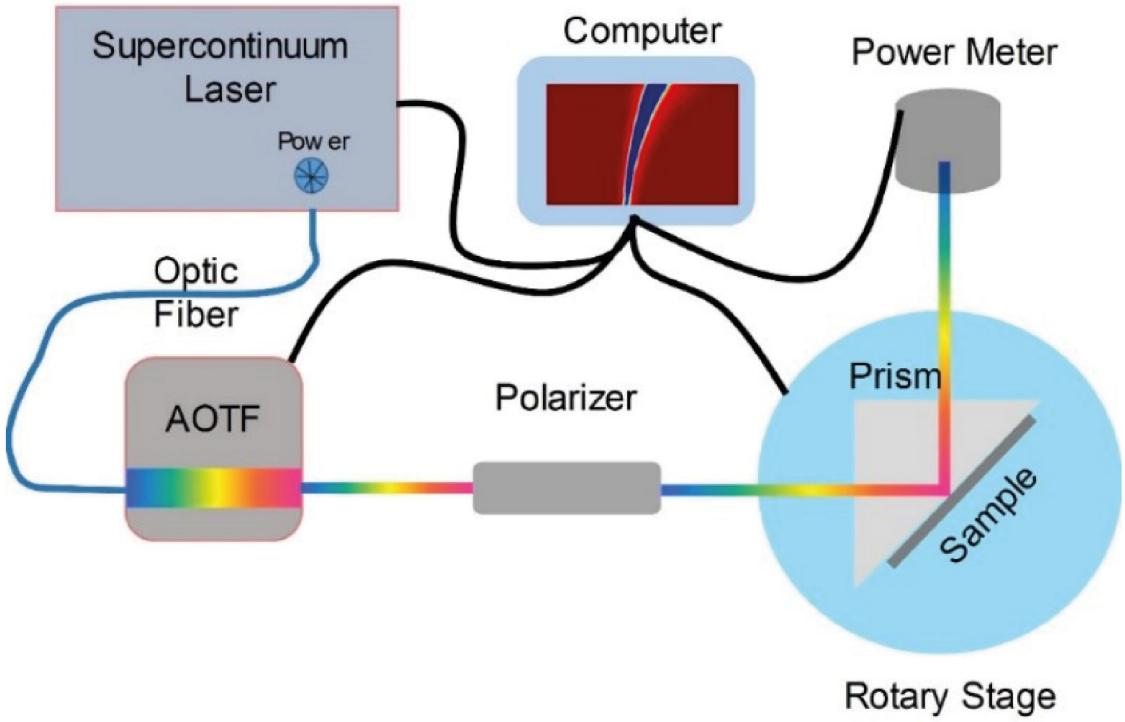

Figure 1.12. Schematic representation of the experimental set up used to investigate surface plasmon polaritons

In this thesis, the Kretschmann configuration shown in figure 1.12 was used to investigate the relationship between different exciton sources that strongly interact with the emitted surface plasmon polaritons (SPPs) of a silver film in the visible spectrum. The light source is a supercontinuum laser (Koheras-SuperK Versa) providing tunable laser light with a spectral width of about 1 nm. This narrow bandwidth ensures precise measurements of the coupled exciton-plasmon modes. The light is further tuned in the visible and near-infrared range using an acousto-optic tunable filter (AOTF), allowing detailed analysis of the coupling over entire spectral range of interest. The incident light is p-polarized to ensure optimal excitation of the SPPs on silver film. A power meter accurately measures the power of the reflected light for each wavelength, allowing detection of the coupled exciton-plasmon modes. Normalization with the s-polarized light further enhances the sensitivity of the measurement to the coupling process. In the strong coupling regime, incident light efficiently binds to SPPs on the thin metal film, leading

to the formation of mixed plasmon-exciton polaritons. This regime is characterized by significant energy transfer between excitons and SPPs, leading to the formation of novel hybrid modes with unique properties.

In chapter 2, surface plasmon-exciton polaritons measured using the Kretschmann configuration are studied in detail.

1.3.3 Hyperspectral Imaging

Hyperspectral Imaging (HSI) is a powerful technology that captures information about an object or scene across a wide range of wavelengths, far beyond what the human eye can see. It goes beyond traditional imaging, which typically captures only three color bands (red, green, and blue). Instead, HSI provides a full spectrum of light for each pixel in the image, creating a data matrix that contains both spatial and spectral information. This allows us to identify and analyse materials based on their unique spectral signatures.

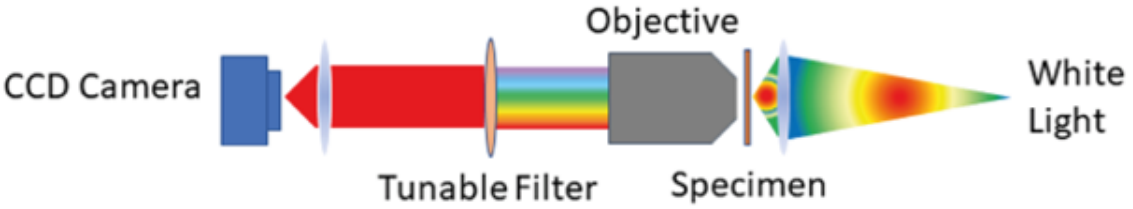

Figure 1.13. Schematic representation of the experimental set up used to investigate surface plasmon polaritons

In this thesis, we will use hyperspectral imaging (HSI) to investigate the intricate details of the light-matter interaction between an exciton source confined in an optical cavity and the cavity photons. This investigation will be conducted through a comprehensive exploration of the spectral and spatial properties associated with this intriguing phenomenon. In order to analyze exciton polariton formation in the microcavity in the spatial domain, a hyperspectral imaging system is used. The imaging system schematically shown in Figure 1.13 includes a broadband white light source, an electrically tunable optical filter, and a CCD camera with different lenses. The electrically tunable liquid crystal filter is a powerful tool for studying the properties of these exciton polaritons, providing a continuously tunable central wavelength in the range of 420 nm to 730 nm with a bandwidth of less than 10 nm.

1.4 Background of Simulation

Finite Difference Time Domain (FDTD) is a tool in the field of computational electromagnetics. It is one of the fundamental building blocks for understanding and analyzing scientific experiments, especially in the field of photonics, allowing us to model in detail the complex interaction of light with matter. By solving Maxwell's equations directly without physical approximations, FDTD produces highly accurate results and allows us to design new materials for complex phenomena such as light scattering, absorption, and emission. This makes it an essential tool for researchers and engineers in a wide range of disciplines, from designing next-generation optical devices to understanding the intricacies of biological processes. In this thesis, the FDTD method was performed using a software called Lumerical, which, as mentioned above, helped us to understand complex phenomena such as light scattering, absorption and emission, and to prepare suitable new samples.

CHAPTER 2

The Strong Coupling Regimes

2.1 Plasmonic Cavities

This chapter focuses on the fascinating area of the strong coupling between plasmonic voids and excitons, in particular the complex interaction between localized surface plasmon resonance (LSPR) and excitons with different optical properties. We present a comprehensive analysis of the interactions between these entities covering a wide range of optical properties and LSPR behavior. In addition, this chapter provides a comprehensive review of the strong coupling between LSPR and excitons in plasmonic nanoparticles by studying different nanoparticle shapes and their corresponding optical properties. This in-depth investigation reveals the profound influence of geometric factors on coupling dynamics and provides insights into the manipulation of light-matter interactions at the nanoscale.

2.1.1 Coupling between Surface Plasmon Polariton and Exciton

In the study of plasmon-exciton coupling (Finkelstein-Shapiro et al., 2021) in CDs (carbon dots) on planar metallic surfaces, the Kretschmann configuration, set up as shown in figure 2.1(a), was used. It is noteworthy that the Kretschmann configuration is a well-established technique for the excitation of surface plasmons on thin metallic films. Incident photons couple to surface plasmons located at the interface of thin metallic films, resulting in the generation of surface plasmon polaritons (SPPs). This resonant excitation occurs when the in-plane momentum of the incident light (k_x) matches the real part of the SPP momentum (k_{SP}), effectively synchronizing the propagation of the SPP with the incident light wave. The angular distribution of the scattered electromagnetic field is governed by the relationship $k_x = k_0 n_p \sin(\theta)$, $k_{SP} = 2\pi/\lambda(\varepsilon_m \varepsilon_d/(\varepsilon_m + \varepsilon_d))^{1/2}$, where n_p is the refractive index of the prism, θ is the angle of incidence of the illuminating light, λ is its wavelength, and ε_m and ε_d are the dielectric constants of the metallic and dielectric

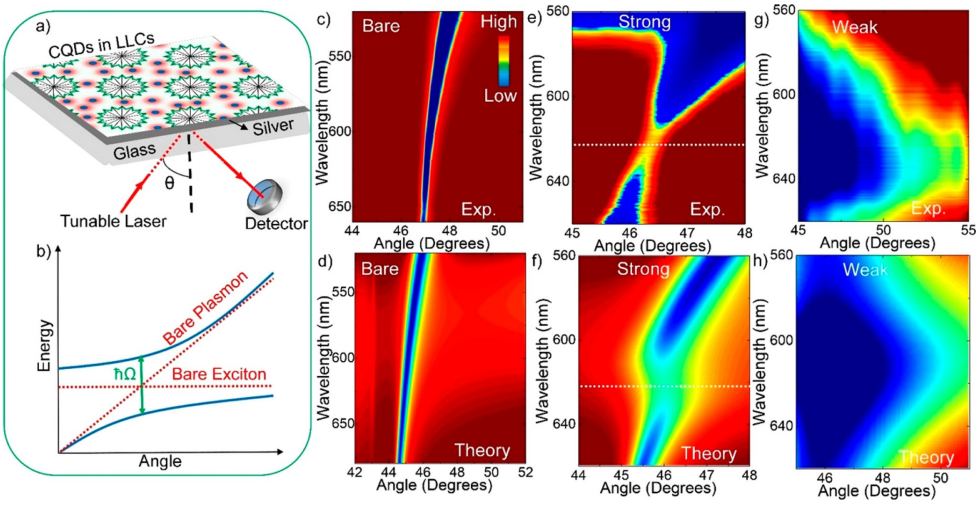

Figure 2.1. The coupling between strong and weak light-matter coupling regimes in carbon quantum dots embedded in liquid crystal mesophases in the vicinity of a metallic thin film. (a) Schematic illustration of the experimental setup used in the Kretschmann configuration for the excitation of surface plasmons on a flat silver film covered with CDs embedded in LLC mesophases. (b) A schematic illustration of the strong coupling phenomenon observed between excitons of carbon dots (CDs) and surface plasmon polaritons (SPPs) of a metal film. (c) Experimental surface plasmon polariton dispersion curve from bare silver. (d)Theoretical surface plasmon polariton dispersion curve from silver film. (e) Experimental dispersion curve of a 60 nm thick silver film with a CDs coating. (f) The polariton dispersion curve of a silver film placed on a Lorentz oscillator with the same resonant wavelength and linewidth as CDs is theoretically demonstrated. (g) Experimental measurement of the dispersion relation for surface plasmons on a 25 nm thick silver film covered by carbon dots (h) The polariton dispersion curve of a 25 nm thick silver film overlaid with a Lorentz oscillator having the same resonance wavelength and line width as the CDs is presented in a theoretical context. Copyright ©American Chemical Society (Sarisozen et al., 2022).

media, respectively. To investigate the coupling between CDs excitons and metal film surface plasmon polaritons (SPPs), polarized reflection measurements were performed across a range of incident angles, as depicted in figure 2.1(b). Additionally, a tunable laser light source with a spectral width of approximately 1 nm was employed to characterize the dispersion curve of a thin Ag film (figure 2.1(c)). Theoretical calculations further confirmed the experimental results shown in figure 2.1(d). In particular, the coverage of the Ag film with CDs in LLC mesophases resulted in an anti-crossover behavior in the dispersion curve. In addition, CDs in water and LLC mesophases exhibit maximum absorption resonance wavelengths centered around 610 and 625 nm, respectively. The observed reverse transition at the peak absorption wavelength of the CDs (625 nm) in figure 2.1e) and f provides compelling evidence for strong coupling between the surface plasmon polaritons (SPPs) of the 60 nm silver film and the excitons of the CDs. The condition for the strong coupling regime between plasmons and excitons is fulfilled when the Rabi splitting energy ($2g$) exceeds half the sum of the exciton (γ_e) and plasmon polariton (γ_{pl})

linewidths, i.e., $2g > (|\gamma_e| + |\gamma_{pl}|)/2$. This is observed in the present case, where $2g \sim 90$ meV, $|\gamma_e| \sim 75$ meV, and $|\gamma_e| \sim 100$ meV for a 60 nm thick Ag film (Zengin et al., 2015), (Khitrova et al., 2006). The experimental results shown in fig.2.1e are demonstrably confirmed by the theoretical predictions shown in figure 2.1(g). Furthermore, there is a direct relationship between the Rabi splitting energy and the number of excitons, with the former increasing in proportion to the square root of the latter (Balci et al., 2012). In figure 2.1(e), despite attempts to increase the separation between the upper and lower polariton branches, this was not achieved due to the accumulation of excess CDs in the liquid crystal. In essence, the liquid crystal has a limited capacity to accommodate embedded CDs. In particular, the linewidth of surface plasmon polaritons in thin metal films can be tuned by adjusting the thickness of the metal film (Balci et al., 2012). For the experimental demonstration of the weak coupling regime between carbon dots and surface plasmon polaritons, the thickness of the silver film was reduced to 25 nm, resulting in a plasmon damping rate (γ_{pl}) of about 300 meV. As shown in figure 2.1(g) and (e), a minimal splitting of the dispersion curve ($2g < |\gamma_e + \gamma_{pl}|/2$) is observed, confirming the weak coupling between the CDs excitons and the surface plasmon polaritons. This is further supported by the complete mapping of the strong CDs absorption peak in the liquid crystal.

The hybridization of localized surface plasmon polaritons (LSPPs) on metal nanoparticles with propagating surface plasmon polaritons (SPPs) on flat metal films can lead to significant shifts in the plasmon resonance frequency and substantial enhancements in the electric field (Balci et al., 2015). These phenomena have significant implications for various applications, including surface-enhanced spectroscopy, strong plasmon-exciton coupling, plasmonic light sources, and solar cells (Moreau et al., 2012), (Mock et al., 2008). For the study of plasmon-plasmon coupling between decahedral nanoparticles and flat metal surfaces, the well-established Kretschmann configuration was used. This configuration is widely used to excite surface plasmons on thin metal films. Figure 2.2(a) shows a schematic illustration of the experimental setup used to study the coupling between localized and propagating surface plasmon polaritons. Spectroscopic reflection measurements as a function of both polarization and angle of incidence were performed to elucidate the coupling behavior between localized and propagating SPPs. A tunable laser light source with a spectral bandwidth of about 1 nm was used to generate the necessary excitation wavelengths for this investigation. To achieve surface plasmon polariton (SPP) formation, the horizontal component of the incident light momentum (k_x) must be equal to the real part of the SPP momentum (k_{SP}). This condition requires a specific dispersion relation, which is given by the equation:

$$k_x = k_0 n_p \sin(\theta) = k_{SP} = 2\pi/\lambda(\varepsilon_m \varepsilon_d/(\varepsilon_m + \varepsilon_d))^{1/2} \tag{2.1}$$

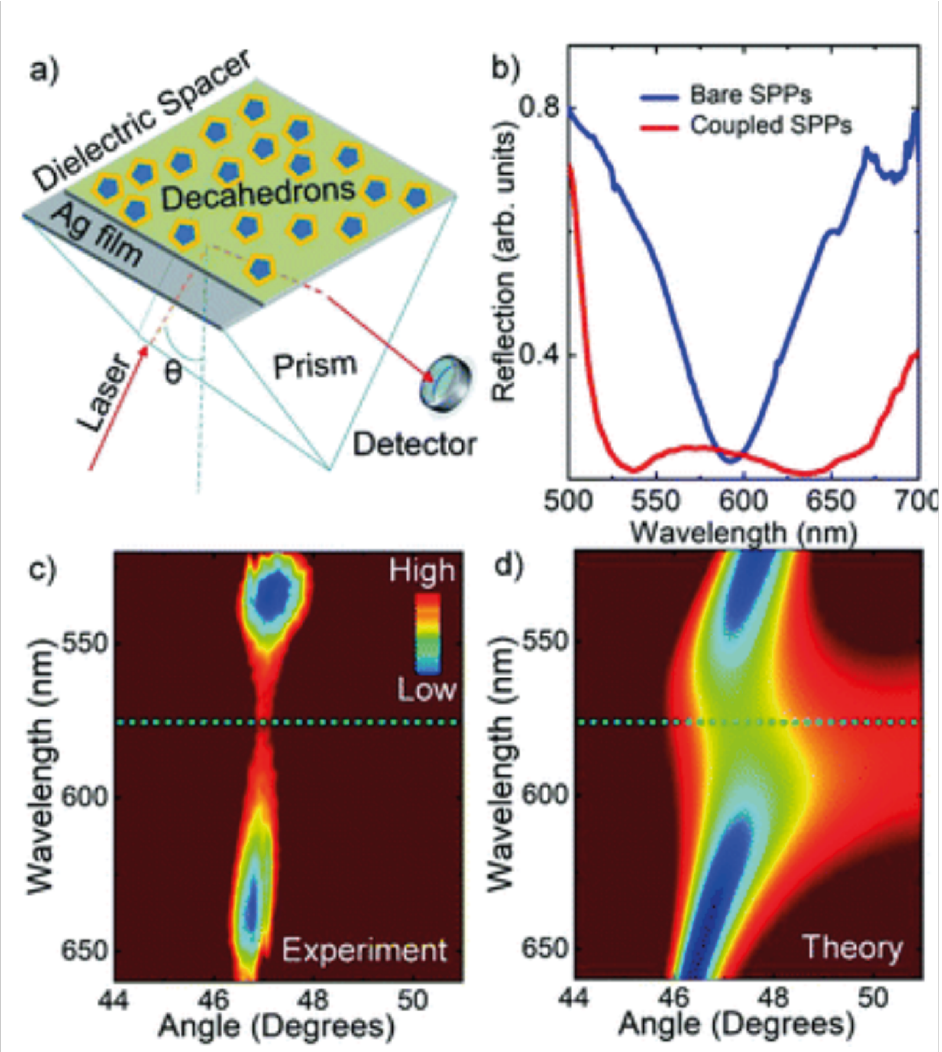

Figure 2.2. Strong plasmonic interactions between bimetallic decahedral nanoparticles and a flat silver substrate. (a) Schematic representation of the Kretschmann configuration for surface plasmon excitation on a silver film. (b) Reflection spectra were recorded for both a bare Ag film and a coupled decahedral NPs-Ag film at an incident angle of about 47 degrees. Under resonant excitation conditions, the reflectivity exhibited a distinct minimum within the dispersion curves as indicated by the blue region. (c) Spatial distribution of decahedral nanoparticles on an Ag film, obtained through experimental methods. (d) The dispersion curve of a Lorentz oscillator, representing the extinction of bare decahedral nanoparticles on the Ag film, is derived theoretically. Copyright ©The Royal Society of Chemistry (Balci et al., 2021).

where, $k_0 n_p$ is the wave number of incident light in the prism ($k_0 n_p = 2\pi n_p/\lambda$), n_p is the refractive index of the prism, θ is the angle of incident light, λ is the wavelength of incident light and ε_m and ε_d are the dielectric constants of metal and dielectric, respectively. This equation is the key to matching the momentum of the incident light to the momentum of the SPP, thereby enabling the excitation of surface plasmons and the formation of SPP waves. Figure 2.2(b) shows the reflectance spectra for both a pure Ag film and a coupled decahedral NPs-Ag film. The dispersion curve for the nanoparticles coupled to the Ag

film is shown in fig.2.2c. It is important to note that the bare Ag film exhibited dispersion without any evidence of anticrossing behavior. The observation of anticrossing behavior in the dispersion curve provides compelling evidence for the strong coupling between the localized surface plasmon polaritons (LSPPs) of the decahedral nanoparticles (NPs) and the propagating surface plasmon polaritons (SPPs) of the Ag film. This interaction leads to the formation of a plasmonic nanocavity characterized by a pronounced gap-dependent plasmon resonance, indicating the strong influence of the interparticle spacing on the collective plasmonic response (Moreau et al., 2012). The resonance wavelength of the nanocavity exhibits a red shift as the gap distance decreases, relative to the resonance wavelength of the isolated metal nanoparticle (Mock et al., 2008). This phenomenon is observed in figure 2.2(c), where the bare decahedral bimetallic nanoparticles exhibit a plasmon resonance around 550 nm, while the coupled nanocavity resonates at around 575 nm. This corresponds to a calculated red shift of about 25 nm. Notably, our previous study (Balci et al., 2015) investigated the coupling between a thin Ag film and Ag nanoprisms with a larger gap distance (> 10 nm), resulting in a minimal difference between the plasmon resonance wavelengths of the isolated and coupled nanoparticles. The experimental observations shown in figure 2.2(c) are confirmed by the theoretical calculations shown in figure 2.2(d). Our theoretical model assumes that the plasmonic nanoparticle behaves as a Lorentz oscillator with a resonance energy of 2.14 eV and a resonance width of 122 meV (details are provided in the electronic supplementary information). This research demonstrates the potential of the described plasmonic nanocavity to study light-matter interactions in a remarkably small volume (approximately 50 x 50 x 5 nm^3) (Chikkaraddy et al., 2016).

The dispersion curve of surface plasmon polaritons (SPPs) in the bare silver film is shown in fig.2.3a. By simply varying the angle of incidence of the laser light, the resonance wavelength of the SPPs can be easily controlled. Fig.2.3b-d show the polariton dispersion curves for perovskite nanocrystals (NCs) coupled to the SPPs, namely CsPb(Br/I)3 nanoplatelets, CsPbI3 nanoplatelets and CsPbI3 nanowires, respectively. The largest Rabi splitting energy was observed for the monohalide CsPbI3 nanoplatelets. This phenomenon can be attributed to lower exciton-phonon coupling in monohalide perovskite NCs compared to their mixed halide counterparts (Weidman et al., 2016). Furthermore, a significant decrease in Rabi splitting energy was observed with increasing dimensionality and quantum size effects, progressing from nanoplatelets to nanowires. In particular, the red-shifted absorption peak observed for CsPbI3 nanowires in fig.2.3c is indicative of the reduced quantum confinement effect in these structures. The calculated Rabi splitting energies extracted from the exciton-polariton dispersion curves are approximately 90 meV, 70 meV, and 55 meV for CsPbI3 nanoplatelets, CsPbI3 nanowires, and CsPb(Br/I)3 nanoplatelets, respectively.

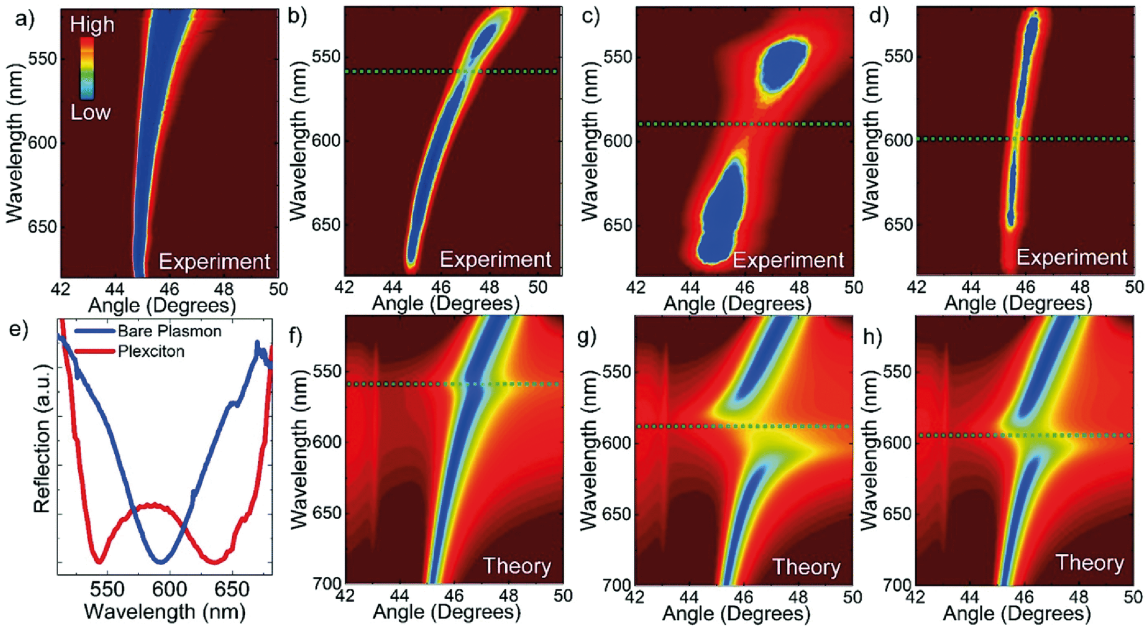

Figure 2.3. Experimental and theoretical dispersion curves of surface plasmon perovskite exciton coupling. (a) Dispersion curve of SPPs from bare silver. (b) Cesium lead bromide/iodide (CsPb(Br/I)3) nanoplatelets, (c) cesium lead iodide (CsPbI3) nanoplatelets, and (d) cesium lead iodide (CsPbI3) nanowires are depicted. The dispersion curves are overlaid with dotted lines showing the energy positions of the unpaired perovskite nanocrystal excitons. (e) as shown in the reflection curves, a bare silver film exhibits a surface plasmon polariton (SPP) resonance with a characteristic wavelength at about 45.5 degrees of incidence. When the silver film is coated with CsPbI3 nanoplatelets, a redshift of the SPP resonance to 46 degrees is observed. Furthermore, both upper and lower polariton branches are clearly visible in the reflection spectra. Theoretically calculated polariton dispersion relations for a silver film decorated with (f) CsPb(Br/I)3 nanoplates, (g) CsPbI3 nanoplates, and (h) CsPbI3 nanowires. Copyright ©The Royal Society of Chemistry (Guvenc et al., 2020).

2.1.2 Coupling between Localized Surface Plasmon and Exciton

Metallic nanoparticles possess the remarkable ability to confine light at subwavelength dimensions through localized surface plasmon polaritons (SPPs), creating promising opportunities for bridging the gap between photonics and electronics at the nanoscale (Yuen-Zhou et al., 2016) (Ozbay, 2006).These hybrid states, formed by strong coupling with incoming photons, are half light and half electron and offer unique properties. In particular, their ability to localize light in small volumes, increase field intensity, and exhibit extreme sensitivity to environmental parameters such as size, shape (Pala et al., 2009), and refractive index has paved the way for numerous critical applications in areas such as surface-enhanced spectroscopy and sensing (Aslan et al., 2007), (Sherry et al., 2006). In addition, due to their nanoscale size, metallic nanoparticles exhibit unique properties that

enable strong localization and manipulation of optical fields. These complex structures can be further exploited in the form of nanoparticle dimers and aggregates, where highly localized and intense optical fields known as plasmonic hotspots (Grésillon et al., 1999) are generated at nanoparticle-nanoparticle interfaces. Plasmonic hotspots have shown tremendous potential in enhancing the fluorescence of dye molecules and quantum dots (Bek et al., 2008), as well as in enhancing the Raman scattering of molecules (Chikkaraddy et al., 2016), (Xu et al., 1999). Furthermore, the optical properties of metallic nanostructures clearly depend on their geometry, size, composition, and the surrounding dielectric environment (Xia et al., 2009).

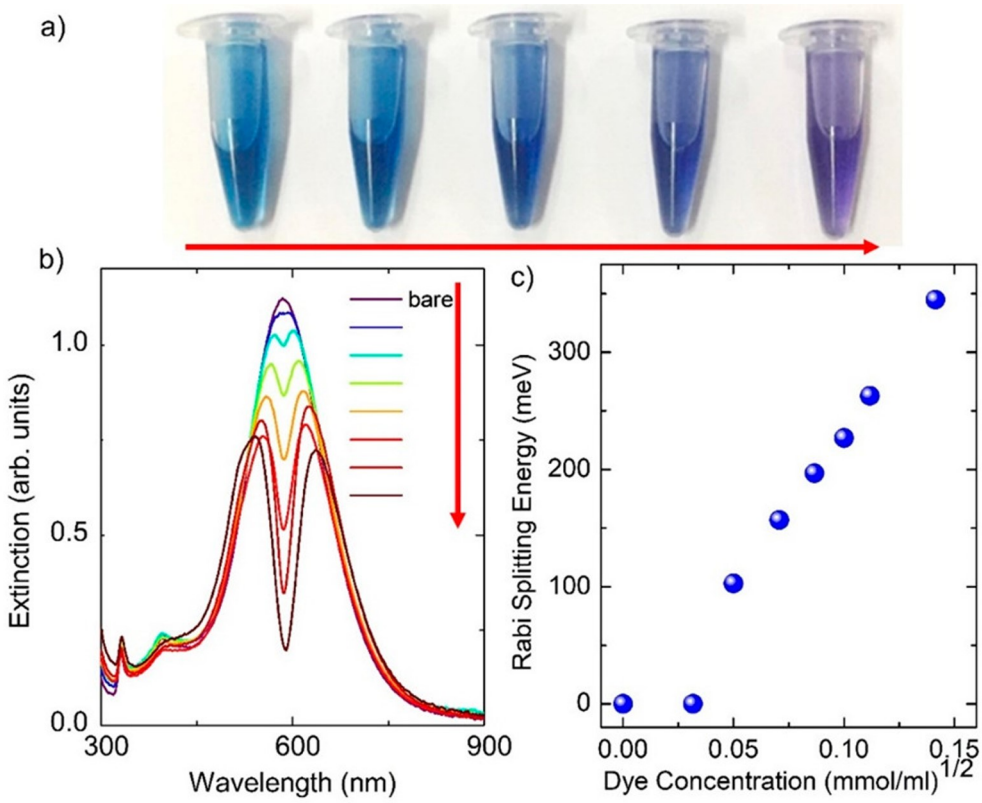

Figure 2.4. The tunable coupling of localized surface plasmons and excitons in nanodisk-shaped plexcitonic nanoparticles. (a) Photo of various concentrations of J-agg dye in the strong coupling regime with silver disks. (b) Investigation of the effect of J-aggregate dye concentration on the plasmonic response of silver nanodisks using extinction spectroscopy. (c) The Rabi splitting energies were calculated for different concentrations of J-aggregated dye on the silver nanodisks. Copyright ©American Chemical Society (Balci et al., 2019).

As shown in figure 2.4, we can precisely control the number of dye molecules (dye concentration) bound to metal nanoparticles by adjusting the number of particles in the dye solution in the reaction medium. A photograph of nanodisc colloids containing J-aggregate dyes at different concentrations is shown in figure 2.4(a). Figure 2.4(b) shows

the profound effect of the strong coupling between the localized surface plasmon resonance (LSPR) and the J-aggregate exciton on the extinction spectra of nanodisc colloids; the dye concentration plays a very important role. Strong exciton-plasmon coupling occurs when the energy transfer rate between exciton and plasmon (g) exceeds both the plasmon decay rate (γ_p) and the exciton decay rate (γ_{ex}) such that $g > \gamma_{p,ex}$ (Tischler et al., 2007). The strong coupling regime allows for a reversible energy transfer between the plasmons and the excitons (Vasa and Lienau, 2018). When In the regime where the energy transfer rate (g) is significantly smaller than the decay rates of both plasmons and excitons ($g < \gamma_{p,ex}$), respectively, weak coupling is observed (Limonov et al., 2017). Figure 2.4(b) clearly shows the transition from the weak binding regime to the strong binding regime.In particular, the Rabi splitting energies exhibit a square root dependence on the number of TDBC molecule (Ribeiro et al., 2018). It is worth emphasizing that the strength of the plasmon-exciton coupling, which is determined by the magnitude of the Rabi splitting energy, is successfully controlled by the amount of dye molecules present in the environment.If one of the coupled oscillators is a Frenkel exciton, the Rabi splitting frequency (Ω) is proportional to the square root of the number of molecules (N) in the medium (Balci et al., 2012). Figure 2.4(c) shows the variation as a function of the number of molecules ($\sqrt{N}$).

To corroborate the experimental data and delve deeper into the genesis of the robust plasmon-exciton coupling observed in the nanodisk-shaped plexcitonic nanoparticle, finite-difference time-domain (FDTD) simulations of a single particle were performed, as shown in fig.2.5a. In the simulation framework, the silver nanodisk was suspended in air ($n_{air} = 1.0$), and the dispersion of the molecular exciton was assumed to follow a Lorentzian profile (Oughstun and Cartwright, 2003), expressed as $\varepsilon(\omega) = \varepsilon_0 + f_0(\omega_0^2/(\omega_0^2 - \omega^2) - i\gamma_0\omega$, where the resonance wavelength of the J-aggregate was set to 587 nm (2.11 eV) and its linewidth (γ_0) was approximately 32 meV.

The self-assembly of J-aggregate dyes on bimetallic nanorings resulted in the formation of plexitonic nanorings. In the strong binding regime, plasmons and excitons interact intensively, leading to the emergence of new hybrid polariton modes. Using the coupled oscillator model, the energies of the upper and lower polariton branches can be expressed as $E_{1,2} = (E_p + E_{ex})/2 \pm 1/2(4g^2 + (E_p - E_{ex})^2)$, where E_1 and E_2 represent the upper and lower polariton energies, g denotes the binding strength, and E_p and E_{ex} denote the plasmon and exciton resonance energies (Balci et al., 2012). When the detuning is zero, the energy difference between the upper and lower polariton branches is defined as the Rabi splitting energy. Strong coupling is achieved when the coupling strength (g) exceeds $(\gamma_p - \gamma_{ex})/2$. To manipulate the coupling strength, we incorporated different amounts of J-aggregate dyes into the nanoring colloid and performed a thorough analysis of the extinction spectra of the hybrid system, as shown in figure 2.6(a-c). The increased quantity of gold ions incorporated into the silver nanodisk in figure 2.6(b) compared to figure 2.6(a) manifests as a prominent interband transition feature within the extinction

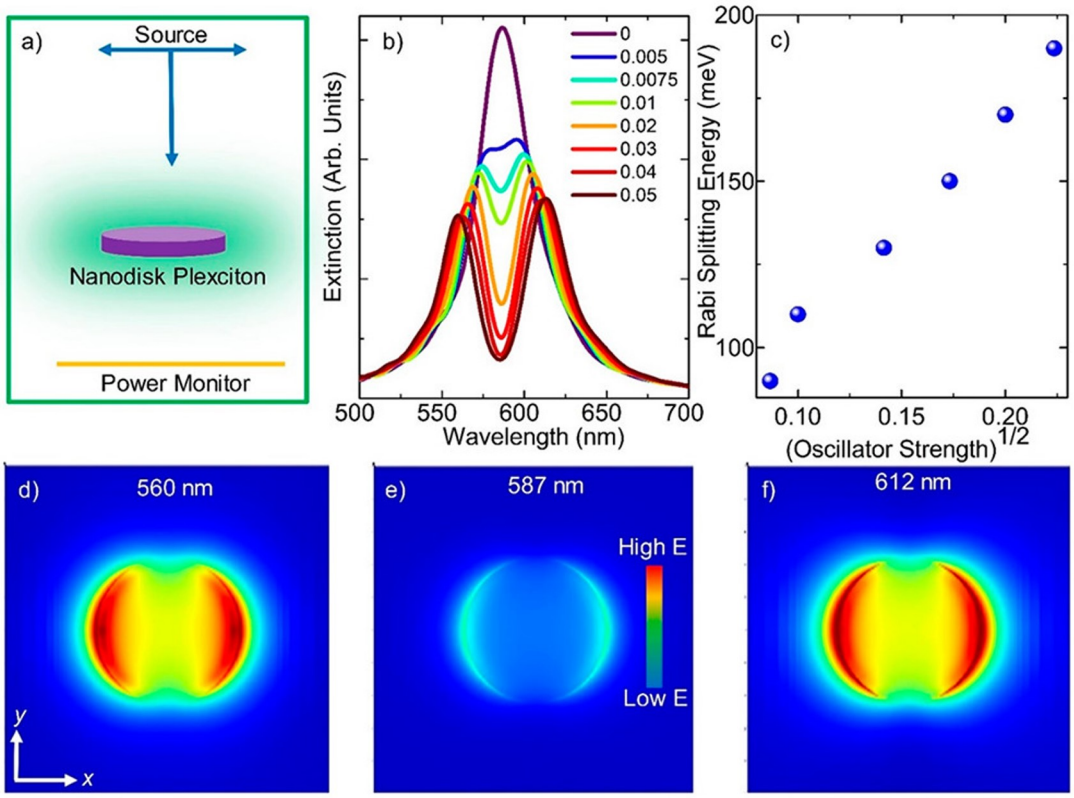

Figure 2.5. Nanodisk-shaped plexcitonic nanoparticle FDTD simulation. a)Schematic of single plexcitonic nanoparticle FDTD simulation.b)Extinction spectra of a single plexcitonic nanodisk obtained by varying the oscillator strength. c)The dependence of Rabi splitting energy on oscillator strength in the range of 0 to 0.05. The spatial distribution of the electric field within individual plexcitonic nanoparticles is investigated at excitation wavelengths of (d) 560 nm, (e) 587 nm, and (f) 612 nm. Copyright ©American Chemical Society (Balci et al., 2019).

curves. Notably, the calculated and experimentally observed interband edge of gold lies approximately at 2.38 eV (Christensen and Seraphin, 1971). Figure 2.6(c) illustrates the relationship between the calculated Rabi splitting energies and the square root of the dye concentration. Figure 2.6(d) and e show theoretical extinction spectra for a plexcitonic nanoparticle with a silver nanoring (d) and a silver-gold alloyed nanoring (e). Figure 2.6(f) shows the Rabi splitting energies obtained from these theoretical calculations.

Theoretical calculations support that plasmonic hotspots can be created in bimetallic nanodiameters by adjusting the inner diameter of the nanodiameter (figure 2.7). In small-diameter holes, the strong coupling in plasmonic hotspots has a minimal effect.The schematic representation shows a single nanoring, figure 2.7 (a). The spectral response shifts to longer wavelengths with increasing nanohole diameter as shown in figure 2.7 (b) and (c). In addition, the 6 nm nanohole exhibits the lowest threshold for the transition from weak to strong coupling (figure 2.7 (d)). Consistent with this observation, the electric field strength and localization within the nanohole are maximized for a diameter of 6 nm (figure 2.7 (d-h)).Considering that the coupling strength (g) is proportional to the

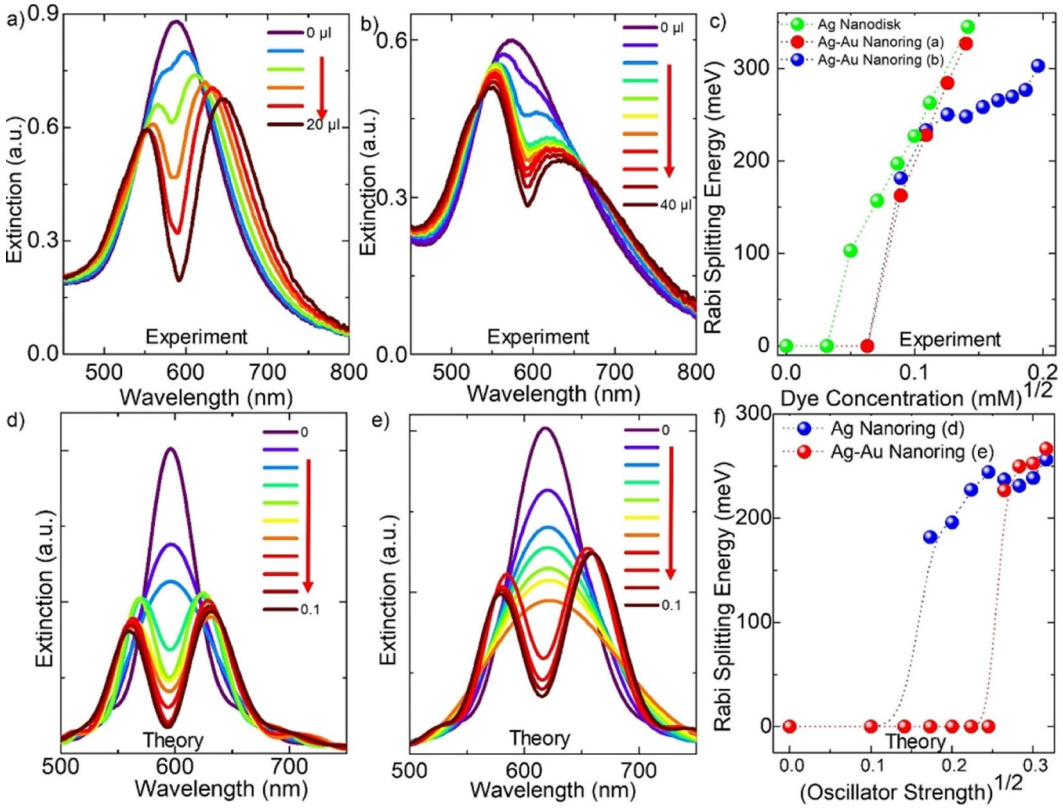

Figure 2.6. The Rabi splitting energy in nanoring-shaped plexcitonic nanoparticles can be precisely tuned. We analyze the modulation of extinction spectra in plexcitonic nanoparticles through the introduction of varying quantities of J-aggregate dye into nanoring colloids with small (a) and large (b) nanoholes. (c) The dependence of Rabi splitting energies on the square root of dye concentration was investigated based on the extinction spectra presented in Figures (a) and (b). The extinction spectra of a nanoring-shaped plexcitonic nanoparticle were theoretically calculated as a function of the dye oscillator strength. This was done for both (d) a silver nanoring and (e) a silver-gold nanoring. Additionally, (f) the Rabi splitting energies were calculated as a function of the square root of the dye oscillator strength.Copyright ©American Chemical Society. (Guvenc et al., 2020).

effective mode volume (V_{eff}) of the cavity, as defined by $\hbar\Omega = 2g - 1/(V_{eff})^{1/2}$, we expect a significant enhancement of the light-matter interaction within these plasmonic nanocavities. Therefore, the gold ion induced nanoholes (6 nm) within the nanodiscs can be definitively classified as plasmonic nanocavities.

The synthesis of decahedral bimetallic plexcitonic nanoparticles was achieved by self-assembly of a J-aggregate dye onto the bimetallic decahedral template. The J-aggregate dye used in this study has an exciton resonance wavelength centered at about 585 nm. Although photochemically synthesized decahedral Ag nanoparticles (figure 2.8 (a)) exhibit a plasmon resonance wavelength of about 490 nm, this spectral feature has insufficient overlap with the exciton transition of J-aggregates in zero tuning. Therefore, we employed a colloidal synthesis strategy involving galvanic exchange reactions to fabricate bimetallic decahedral plasmonic nanoparticles and achieved the desired spectral overlap

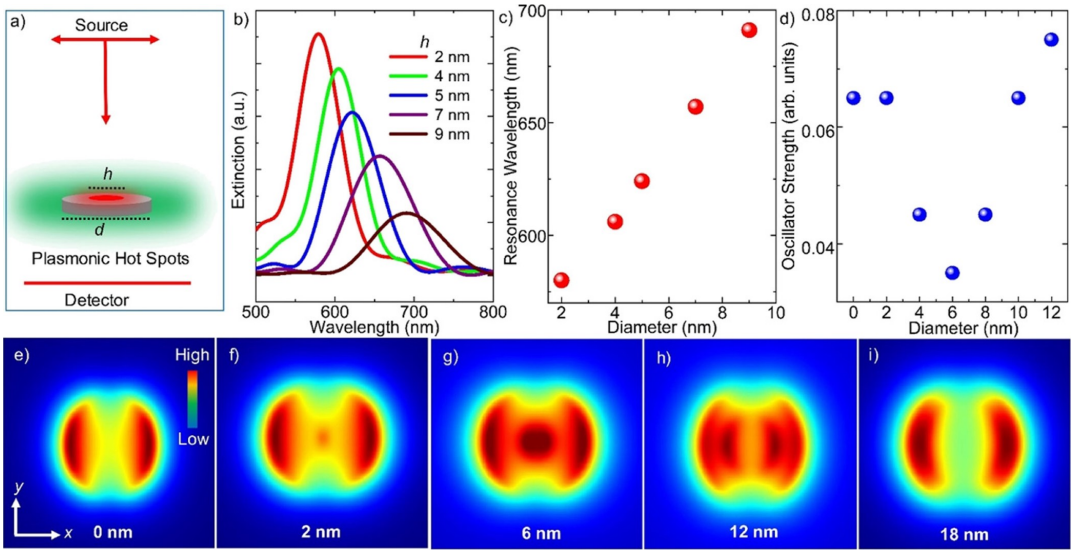

Figure 2.7. Simulation of the optical properties of nanorings with central holes. Figure (a) shows a schematic representation of the simulated nanoring structure. Figures (b) and (c) show the theoretically calculated extinction spectra for increasing nanohole diameters (2-9 nm). Figure (d) analyzes the transition from weak to strong coupling as a function of nanohole diameter (0-12 nm). Finally, figures (e)-(i) visualize the electric field distribution of a single nanohole at its resonance wavelength with varying inner diameters (0-18 nm).Copyright ©American Chemical Society (Guvenc et al., 2020).

as shown by the extinction spectrum in figure 2.8 (b). The observed splitting in the extinction spectrum of the hybrid nanoparticle, especially at the J-agg exciton resonance wavelength shown in figure 2.8 (c), serves as a clear indication of the strong interaction between the localized plasmons of the dodecahedral nanoparticles and the excitons of the J-aggregate dye. Furthermore, theoretical calculations were performed to determine the extinction spectra of the tetrahedral Ag nanoparticles, the tetrahedral Ag-Au alloy nanoparticles, and the tetrahedral Ag-Au plasmon-exciton coupled nanoparticles as shown in figure 2.8 (d-f). In the numerical calculations, the metallic nanoparticle with decahedral geometry was assumed to be suspended in an air medium. The localized Frenkel exciton of the J-aggregate dye was modeled as a Lorentzian oscillator described by the following dielectric function: $\varepsilon(\omega) = \varepsilon_0 + f_0(\omega_0^2/(\omega_0^2 - \omega^2) - i\gamma_0\omega$, where ω_0 represents the resonance frequency of the oscillator, set to 2.1 eV (585 nm), γ_0 is the exciton resonance width, set to about 32 meV, and ε_0 is the background refractive index, set to 2.1. The oscillator strength, f_0, was assumed to be zero for an isolated plasmonic nanoparticle and was varied for coupled nanoparticles.The pronounced spectral minimum observed in figure 2.8 (f) is indicative of strong light-matter coupling, suggesting a highly interacting exciton-plasmon system. The tetrahedral metallic nanoparticles presented in this work exhibit a unique ability to localize electromagnetic waves in an extremely small region at their sharp corners, as shown in figure 2.8 (d). This results from the inverse ratio between the binding strength (g) and the square root of the effective mode volume (V_{eff}) of the

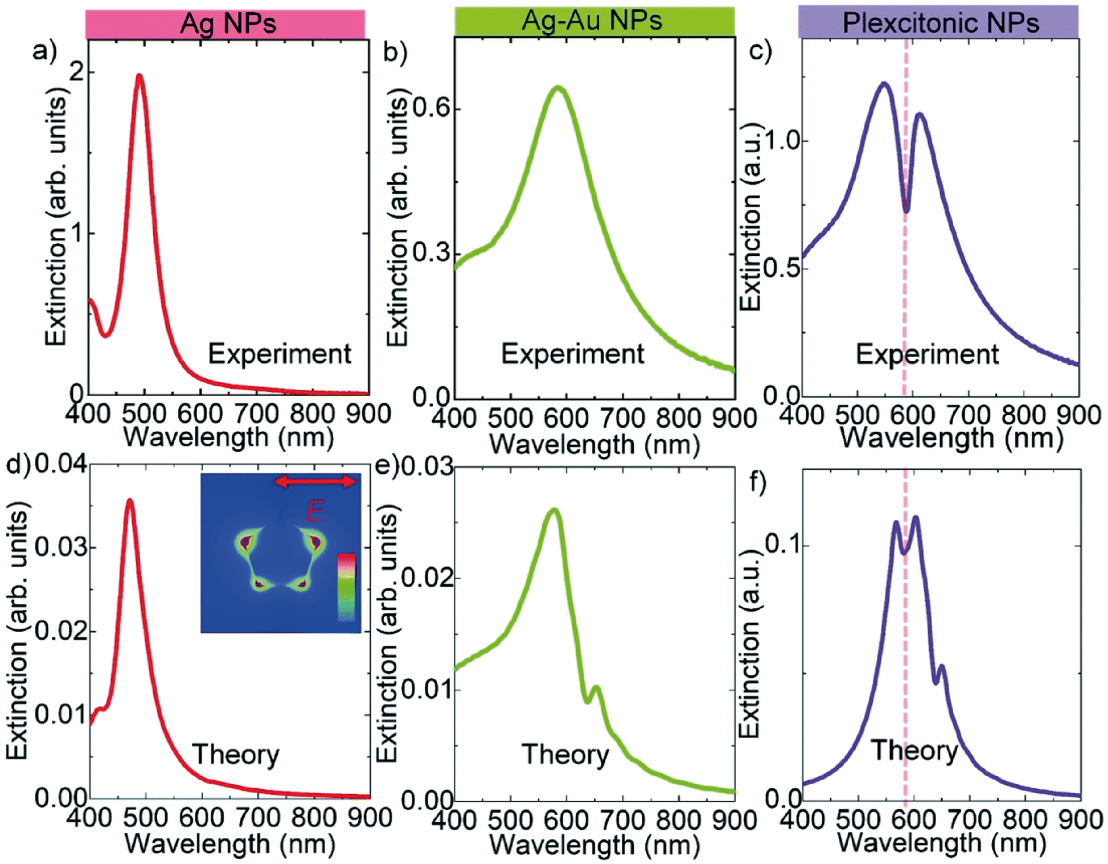

Figure 2.8. The extinction spectra of decahedral-shaped nanoparticles demonstrate strong plasmon–exciton coupling. (a) displays the extinction spectrum of monometallic decahedral Ag nanoparticles in water. (b) shows the extinction spectra of decahedral Ag–Au bimetallic nanoparticles and (c) decahedral Ag–Au plexcitonic nanoparticles. (d), (e), and (f) depict the theoretically calculated extinction spectra for a decahedral Ag nanoparticle, a decahedral Ag–Au nanoparticle, and a decahedral Ag–Au plexcitonic nanoparticle, respectively. Copyright ©The Royal Society of Chemistry (Balci et al., 2021).

cavity. As a result, we expect a significant increase in light-matter interaction at the sharp corners of these tetrahedral plasmonic nanoparticles. This demonstrates their potential to explore light-matter interactions in highly confined spaces, such as strong single-molecule coupling at room temperature (Chikkaraddy et al., 2016). Employing a coupled oscillator model analogous to that utilized for nano-disks and nano-rings, upper and lower polaritons of plexcitons with energies E_1 and E_2 are generated.

2.2 Optical Cavities

Photons can be confined in optical microcavities both spectrally and spatially, which allows us to study light-matter interaction in both weak and strong coupling regimes.

While the former is identified by the Purcell factor, which quantifies the suppression or the enhancement of the spontaneous emission rate of the quantum emitters coupled to the cavity modes, the latter is identified by the formation of hybrid photon-matter modes called exciton polaritons and thus represents an avoided crossing in the spectra. Until now, various imaging and spectroscopic techniques have been extensively used to study exciton polariton formation in optical microcavities and the coupling between excitons and photons has been statically and dynamically tuned. Herein, for the first time, we demonstrate hyperspectral imaging of exciton polaritons in optical microcavities. Two metal thin films acting as reflectors and a polymer matrix containing a collection of quantum emitters form the hybrid system for polariton imaging. We show strong exciton-photon interaction between photons confined in the microcavity and Frenkel excitons of dye molecules placed inside the optical microcavity. We find that exciton polaritons can be imaged and spatially mapped out in the optical microcavity by using hyperspectral imaging in the visible region. We envision that our findings will help to understand exciton polariton formation in the spectral and spatial domains at the same time across different coupling regimes.

2.2.1 Exciton Polaritons in Optical Microcavity

Optical microcavities can confine photons both spectrally and spatially enabling us to study light-matter interactions in both the weak and strong coupling regimes in a wide range of wavelength regions, from visible to microwave wavelengths (Ergoktas et al., 2022). In the weak coupling regime where the coupling strength g between the light and matter is much smaller than the decay rates of the cavity γ_c and the decay rates of the matter $\gamma_m (i.e., g \ll \gamma_c, \gamma_m)$, the energy is lost from the system before it can be transferred between light and matter since the losses in the cavity is larger than the periodic exchange of energy between light and matter. In this regime, modification of the quantum emitter spontaneous emission rate (Purcell effect) owing to the weak interaction with the local density of states is observed, and typically accompanied a slight change in the character of the resonance spectra (Limonov et al., 2017). On the other hand, in the strong coupling regime ($g > \gamma_c, \gamma_m$), the interaction between confined photons in cavities and excitons in semiconductors is coherent and so strong that the new hybrid states or quasiparticles known as exciton polaritons form. In this regime, the periodic exchange of energy quanta between matter and light, known as Rabi oscillations, is observed. The exciton polaritons exhibit distinct physical properties, which are different from light or excitons that form them. For example, polaritons can exhibit superfluidity

(Lerario et al., 2017), and Bose-Einstein condensation at relatively high temperatures (Sun et al., 2017). Incorporating polaritons into optoelectronic devices enables technological advances such as threshold-less polariton lasing (Christopoulos et al., 2007), (Gibbs et al., 2011) engineered polariton bistability (Rodriguez et al., 2016), and a possible pathway to polariton condensation (Balili et al., 2007). In optical microcavities, strong coupling has been commonly studied by using two types of exciton sources: Frenkel excitons, which are typically found in organic materials such as dye molecules, are indeed generated by the delocalization of electrons across the molecule, and Wannier-Mott excitons, which are commonly found in inorganic materials, are forged by the Coulomb interaction between an electron and a hole (Klingshirn, 2012). The choice of exciton source can affect the properties of the resulting exciton polaritons and the coupling strength with the cavity photons (Baranov et al., 2018). In fact, Frenkel excitons in organic microcavities can exhibit large Rabi splitting energies due to their large binding energies resulting from the spatial overlap of the electron and hole wave functions within the organic molecules (Kéna-Cohen et al., 2013),(Kéna-Cohen et al., 2008),(Lidzey et al., 2000),(Lidzey et al., 1998). The initial investigations on exciton polaritons were conducted on GaAlAs/AlAs quantum wells at cryogenic temperatures (Weisbuch et al., 1992). Room-temperature exciton polaritons were firstly discovered in the studies of organic molecules (Lidzey et al., 1998),(Agranovich et al., 2003). Additionally, owing to the rapid rise of two-dimensional materials in photonics, exciton polaritons have been observed by using transition metal dichalcogenides (TMDCs) such as MoS_2, and WSe_2, which have strong in-plane ionic-covalent bonds and very weak out of-plane bonds (Liu et al., 2015). To observe the strong coupling regime in microcavities, it is crucial to precisely tune the cavity photon energy to match the resonance energy of the excitons placed inside the optical microcavity. For example, in recent studies (Junginger et al., 2020), (Nosrati et al., 2021) in the strong coupling regime, a piezo actuator has been successfully utilized to modify the detuning from an optical cavity resonance by adjusting the distance between the cavity mirrors. This manipulation allows observation of strong coupling regime in the microcavities and facilitates the study of the interaction between different photon energies in the microcavity and the excitonic source within the optical cavity. Additionally, a fiber-based Fabry-Perot microcavity has been used to observe strong coupling regime (Gebhardt et al., 2019). In fact, in the previous studies, the strong coupling between excitons and photons has been statically and dynamically tuned and various spectroscopic techniques (mostly optical transmission and photoluminescence measurements) have been commonly used to study exciton polaritons. Herein, we demonstrate hyperspectral imaging of exciton polaritons in an optical microcavity. Hyperspectral imaging is a sample characterization technique utilized for obtaining spectral information from each pixel of the image (Goetz et al., 1985). While hyperspectral imaging was originally developed and used for remote sensing applications in astronomy (mostly in earth surface imaging), in later studies, it

has been widely used in variety of critical applications including food safety, military defense, medicine, archeology, etc. (Faraji-Dana et al., 2019). In this study, we show spatial mapping of strong exciton photon interaction between photons confined in the microcavity and excitons of dye molecules placed inside the optical microcavity by using hyperspectral imaging technique in the visible region (figure 2.9). We find that exciton polaritons can be directly imaged and spatially mapped out in the optical microcavity. Our findings will help to deeply understand exciton polariton formation in both spectral and spatial domains in various coupling regimes in the visible region of the electromagnetic spectrum.

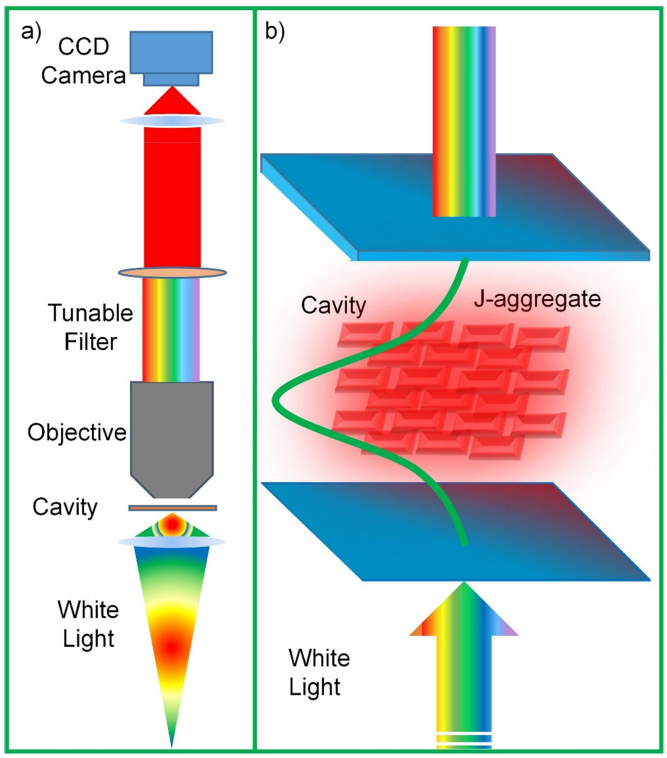

Figure 2.9. Schematic representation of hyperspectral imaging of polaritons in a microcavity. (a) Schematic representation of the hyperspectral imaging system. (b) Schematic representation of direct observation of exciton polaritons in a microcavity. The optical cavity consists of two thin silver mirrors separated by an insulator layer, a thin polymer film. The separation between the silver mirrors allows us to control the optical resonance state of the microcavity. J-aggregate molecules embedded in a thin polymer layer are placed between the silver mirrors. In the hyperspectral imaging system, white light from a broadband source is sent to the sample and the light collected with the objective is sent to the CCD camera. In the strong coupling regime, exciton polaritons are formed inside the optical cavity.

In order to analyze exciton polariton formation in the microcavity in the spatial domain, a hyperspectral imaging system is used. The imaging system schematically

shown in figure 2.9 includes a broadband white light source, an electrically tunable optical filter, and a CCD camera with different lenses. The electrically tunable liquid crystal filter is a powerful tool for studying the properties of these exciton polaritons, providing a continuously tunable central wavelength in the range of 420 nm to 730 nm with a bandwidth of less than 10 nm. The optical microcavity consists of two thin silver mirrors separated by an insulator layer, a thin Poly(vinyl alcohol) (PVA) film. The separation between the silver mirrors enables control of the resonance frequency of the microcavity. Importantly, the two silver mirrors have partially reflective surfaces perpendicular to the longitudinal axis of the system and hence some portion of visible light passes through them, which is necessary for imaging the microcavity mirror surface. J-aggregate molecules embedded in the PVA polymer layer are placed between the two silver mirrors. In the hyperspectral imaging system, the white light from a broadband source is sent to the sample through a polarizer and a condensing lens. The transmitted light is collected by the objective and directed to the CCD camera by following the optical path schematically shown in figure 2.9 (a). The CCD camera captures the image of the sample for each central wavelength. The images are then analyzed to discover the spectral and spatial signatures, which help quantify the interaction of the cavity field with the J-aggregate molecules.

Hyperspectral imaging of the bare optical microcavity, composed of two partially reflective Ag mirrors separated by a thin layer of PVA, is shown in figure 2.10. The resonance condition for such a cavity can be written as $2nd = m\lambda$ where m is an integer, λ denotes the resonance wavelength, n is the refractive index of the medium between the mirrors, and d is the distance between the mirrors (nd is the optical path length between the mirrors). Any variation in nd will reflect itself as a change in the resonance frequency. This is clearly seen in the colored map of optical transmission of the microcavity in the spatial domain (figure 2.10 (b)), implying that the optical path length through the PVA layer between the mirrors is not constant. In fact, the imaging system detects optical response (transmission or reflection) of the sample over the visible spectral band for each pixel within the image. The variation originates from the spin coating process used to form the PVA layer on the silver mirror surface. The fluctuation of the PVA layer thickness is reflected in the color map as the variation of the cavity resonance frequency. In figure 2.10 (a), the optical microcavity has been successfully mapped out by using hyperspectral imaging system. The transmission spectra of the microcavity mapped out from the acquired hyperspectral image along the white arrow in figure 2.10 (b) is shown in figure 2.10 (c), which shows a good agreement with the results obtained from finite difference time domain (FDTD) simulations of the cavity (figure 2.10 (d)). It should be noted that the lateral distance across the arrow in figure 2.10 (b) is converted to the cavity size by finding the resonance wavelength of the each data point on the white arrow.

We now turn our attention to optical microcavity filled with J-aggregate dyes embedded in the PVA layer, figure 2.11(a). The strong coupling of excitons and photons

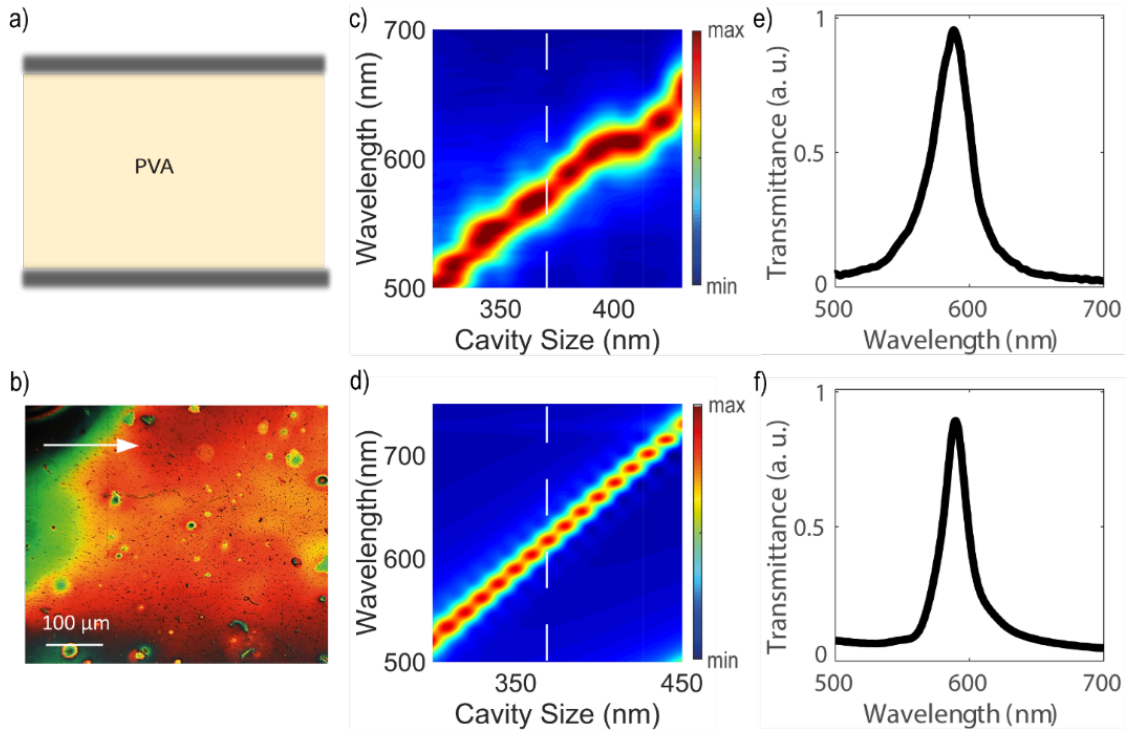

Figure 2.10. Hyperspectral imaging of a bare optical microcavity. (a) Schematic representation of the optical cavity consisting of two partially reflective Ag mirrors separated by a thin layer of PVA. (b) Hyperspectral image of the cavity. Each pixel in the hyperspectral image exhibits the transmission spectrum through the cavity. Different color shades seen in the image is due to the variation in the PVA layer thickness within the cavity. (c) Experimental dispersion curve of a bare optical cavity (wavelength vs cavity size). Two dimensional map extracted from the region along the white arrow, in (b), shows the correlation between the resonance of the cavity and the cavity size. (d) Theoretical dispersion curve of a bare optical microcavity. (e) Experimental transmittance spectrum extracted from the dashed line in (c). (f) Theoretical transmittance spectrum extracted from the dashed line shown in (d).

in a microcavity can be depicted as the interaction between excitons in the semiconducting material and photons confined in the microcavity, leading to the formation of a composite quantum system known as exciton polaritons. The resonant frequency of the microcavity can be easily fine-tuned by changing the cavity size (i.e., separation of the metal mirrors), which in turn controls the energy levels of the excitons and photons and the new eigenstates that are created. These eigenstates are described as upper and lower polaritons and are separated by an energy splitting known as the Rabi splitting (ω), which indicates the strength of the coupling between photons of the microcavity and excitons of the semiconductor. In this study, for the first time, exciton polariton formation has been directly imaged by using hyperspectral imaging, figure 2.11 (b). The dispersion curve in figure 2.11 (c) showing an avoided crossing is obtained along the white arrow in figure 2.11 (b). The separation of the upper and lower polariton branches at the zero detuning gives information about the value of the Rabi splitting energy, which can be calculated

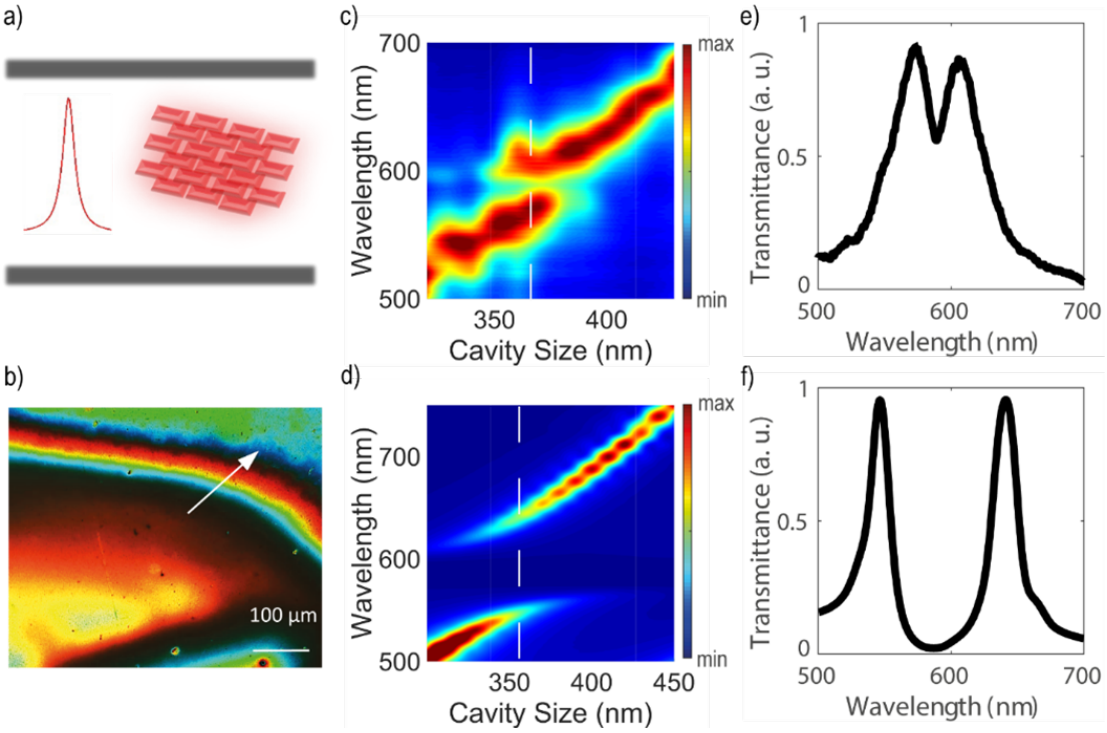

Figure 2.11. Hyperspectral imaging of exciton-polaritons in an optical microcavity. (a) A schematic illustration of an optical cavity consisting of a polymer matrix interspersed with J-aggregate molecules sandwiched between two partially reflecting silver mirrors. (b) A hyperspectral image of the optical cavity filled with J-aggregates. The colored image shows the resonance wavelength of the cavity mode interacting with excitons at each location and, in fact, each pixel of the image represents a transmission spectrum of the optical cavity filled with J-aggregates. (c) Experimentally and (d) theoretically obtained dispersion curves (cavity size vs wavelength) of polaritons. An avoided crossing is observed in the experimental and theoretical dispersion curves. (e) Experimental and (f) theoretical transmittance spectra obtained from the dashed lines in (c) and (d), respectively.

from the dispersion curve as around 200 meV. Figure 2.11 (d) depicts the dispersion curves (cavity size vs wavelength) of polaritons obtained using FDTD simulations. Furthermore, the experimental and theoretical transmission spectra obtained from the dashed lines in figure 2.11 (c) and (d), are shown in figure 2.11 (e) and figure 2.11 (d), respectively. In the simulation, J-aggregate is modelled according to the Lorentz model, which is implemented to produce a material with the following relative permittivity: a resonance linewidth of 32 meV, a resonance of 2.1 eV (587 nm), and a molecular permittivity of 2.04 ($\sim n_{PVA}^2$). It is essential to ensure that the size of the cavity aligns with the resonance wavelength of the cavity photon and the exciton of J-aggregate, as illustrated by the equation $2nL\cos\theta = m\lambda$ represents the wavelength of the cavity resonance, m denotes the number of modes for the cavity, L signifies the size of the cavity, n represents the refractive index of the cavity, and θ is set to zero for our system). Therefore, it is necessary to keep the cavity size at around 300 nm to observe the initial cavity mode.

We now analytically calculate the strong interaction between excitons and photons

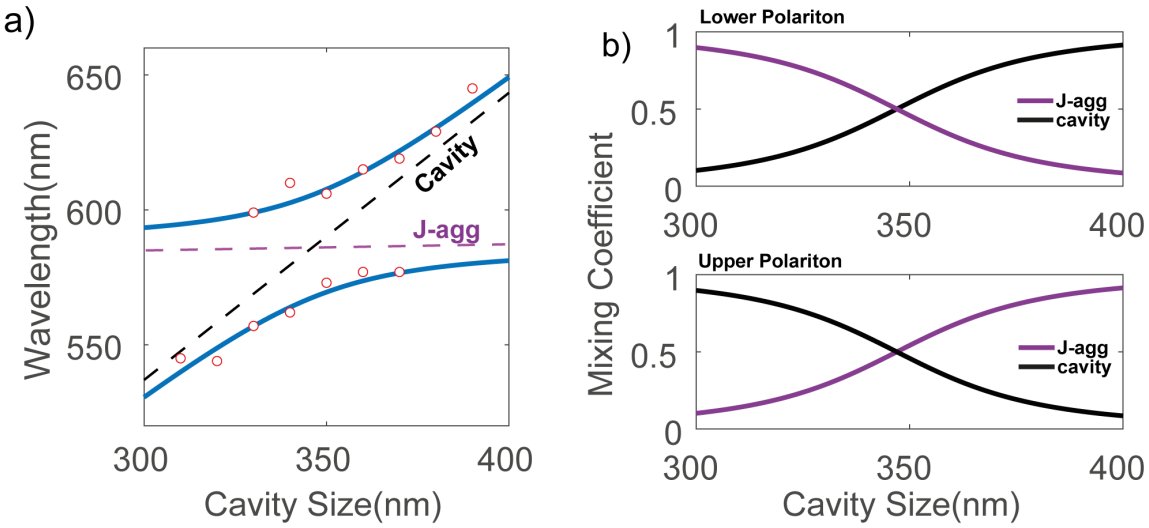

Figure 2.12. Microcavity polariton dispersion and mixing coefficients. (a) The experimental results (circles) show the dispersion curve of polaritons that arise from the strong interaction of cavity photons and J-aggregate excitons. The dashed black line shows how the bare cavity resonance wavelength is modified with the cavity dimensions. The purple dashed line demonstrates the resonance wavelength (~585 nm) of the J-aggregate exciton. (b) The graphs are probability plots showing the relative contribution of the cavity photon and J-aggregate exciton components of the polariton. Lower polaritons have an initial excitonic character and they later change to a photon-like nature (vice versa for the upper polaritons).

inside the optical microcavity. The Jaynes-Cummings (JC) model consists of a two-level system coupled to a single-mode microcavity with bright and narrow linewidth emission (Jaynes and Cummings, 1963). Although the JC model is applicable to a system consisting of a single molecule with a two-level structure, it is not sufficient to fully explain our system, because the Frenkel excitons in the J-aggregates consist of collection of TDBC molecules. Therefore, the Tavis-Cummings model (Tavis and Cummings, 1968) is better suited to our system because it describes the system as a collection of two-level systems that do not interact with each other but are collectively coupled to an optical cavity mode. The Tavis-Cummings Hamiltonian of the strongly coupled system can be defined as follows (Ribeiro et al., 2018),

$$H = \hbar\omega_c a^\dagger a + \hbar\omega_e \sigma^\dagger \sigma + \hbar g\sqrt{N}\left(a^\dagger \sigma + a\sigma^\dagger\right) \tag{2.2}$$

with $\sigma = \frac{1}{\sqrt{N}} \sum_{i=1}^{N} \sigma^{(i)}$, where ω_c and ω_e represent the resonance wavelengths of the bare cavity and exciton, respectively, $a^\dagger$, a and $\sigma^\dagger$, σ are creation and annihilation operators for cavity photon and a material excitation, respectively, g is the interaction parameter between the cavity photon and exciton, and N is the number of molecules in the cavity.

The first and second terms in equation 2.2 describes the energies of the cavity photons and, the exciton, respectively. The third term of the equation involves the interaction between the cavity photon and the exciton. The matrix representation of the interaction Hamiltonian is given as:

$$\begin{pmatrix} \omega_c & \sqrt{N}g \\ \sqrt{N}g & \omega_e \end{pmatrix} \begin{pmatrix} c_+ \\ c_- \end{pmatrix} = \omega_\pm \begin{pmatrix} c_+ \\ c_- \end{pmatrix}. \tag{2.3}$$

By solving for the electronic energy levels of the coupled system, one can obtain both the eigenvalues and eigenstates. The eigenstates of the equation correspond to the combinations of bare states, photonic modes, and excitons, which are collectively called polaritons. The coefficients c_+^2 and c_-^2 denote the probabilities of the photonic and excitonic components, which form the exciton polaritons, respectively, see fig.2.12b. The eigenvalues of (eq.2.3) correspond to the upper (ω_+) and lower (ω_-) polariton branches, which is given as:

$$\omega_\pm = \frac{\omega_c + \omega_e}{2} \pm \frac{1}{2}\sqrt{4Ng^2 + \left(\frac{\omega_c - \omega_e}{2}\right)^2} \tag{2.4}$$

By tuning the cavity resonance frequency (ω_c), the polariton dispersion curve is generated and shown in fig.2.12a. At zero detuning ($\omega_c = \omega_e$), the Rabi splitting energy is given as given as $g\sqrt{N}$ where N is the number of molecules inside the cavity contributing the process (Balci et al., 2019).

2.3 Conclusion

In conclusion, for the first time, we demonstrate hyperspectral imaging of exciton polaritons in optical microcavities. Two metal thin films acting as reflectors and a polymer matrix containing collection of quantum emitters form the optical microcavity. We find that exciton polaritons can be spatially and spectrally mapped out in the optical microcavity by using hyperspectral imaging measurements in the visible region. We envision that our findings will help to develop new tunable nanophotonic systems and devices at nanoscale dimension. Most importantly, we now have a better understanding of exciton polariton formation in the spectral and spatial domains at the same time across different coupling regimes. We note that the same spatial imaging can be performed in the infrared region

of the electromagnetic spectrum as well.

CHAPTER 3

The Weak Coupling Regimes

3.1 Fano Resonance

Fano resonance is a phenomenon that occurs when light interacts destructively with matter due to the interference of two optical paths with different properties. One path is narrow and discrete, while the other is broad and continuous. This interference results in an asymmetric spectral line shape that deviates from the typical Lorentzian profile. Asymmetric line shapes are observable in scattering, transmission, and reflection measurements of weak light-matter interactions in resonant optical systems. This study investigates the interaction between an excitonic nanoparticle and background scattering on the surface of a prism. The objective is to obtain Fano resonance and to study the effects of manipulating background scattering with evanescent waves on the Fano resonance. We studied the impact of altering nanoparticle size and exciton resonance line width on the Fano resonance. Our results indicate that Fano resonances have the potential to regulate light-matter interactions in various applications. This research can open up new possibilities for advancements in photonic devices and systems.

The study of light-matter interactions is an important area in photonics, with particular emphasis on the study of strong and weak coupling regimes. The strong coupling regime is a notable aspect of this field, Rabi splitting (Khitrova et al., 2006) and the resulting new quasiparticles (polaritons) (Byrnes et al., 2014) often occupy an important area in photonics and have been studied extensively. The study of the weak coupling regime is another remarkable part of photonics and is widely recognized as a fundamental area of research. This extensive field is the most popular areas of research, emerging from the fundamental model of weakly coupled two oscillators such as the Fano resonance (Fano, 1961), electromagnetically induced transparency (EIT) (Boller et al., 1991), Borrmann effect (Borrmann, 1950), and Kerker effect (Kerker et al., 1983). The study of the weak coupling regime has allowed the emergence of fundamental phenomena, each with its own unique properties and applications (Limonov, 2021). In weakly coupled interactions, the Fano resonance is a very important and distinctive phenomenon defined by its unique and asymmetric profile resulting from the interaction between discrete and continuous states

(Fano, 1961). Fano resonance manifests itself in a wide variety of photonic phenomena, such as photonic crystal (Yang et al., 2012), (Markoš, 2015), whispering gallery mode resonator (Lei et al., 2014), plasmonic nanostructures (Rahmani et al., 2013), dielectric nanoparticle (Miroshnichenko and Kivshar, 2012), allowing for comprehensive studies in various fields such as optical switching (Nozaki et al., 2013), photoelectric modulators (Zhang et al., 2018), sensors (Zhang et al., 2011), SERS applications (Ye et al., 2012) and Fano lasers (Yu et al., 2017). As mentioned earlier, Fano resonance refers to the interaction of two pairs of oscillators, each with different characteristics. One oscillator has a discrete energy level, a narrow spectral response and a clearly defined local state, while the other oscillator has several energy levels, a broad spectral profile and a continuous broadband state (Joe et al., 2006),(Miroshnichenko et al., 2010),(Limonov et al., 2017). The spectrum of the discrete and continuous states can be caused by different optical phenomena. The discrete state can be detected with electric dipole, transmission, reflection, and extinction spectra (Limonov, 2021). In contrast, the continuum state can be observed by a number of optical phenomena, including subradiative hybrid modes (Cai et al., 2015), broadly localized surface plasmon resonance (Zhang et al., 2006), and background scattering (Fan et al., 2014). In some resonator (Lee et al., 2005) and Mie scattering (Rybin et al., 2013) scenarios, the interference required for the Fano resonance to occur may be due to the interaction between similar modes. A significant case of Fano resonance in Mie scattering arises from interference between dipolar and quadrupolar (or higher order) modes, leading to a narrow resonance that covers a broad background scattering profile (Rybin et al., 2013) . Furthermore, the Fano resonance phenomenon can be induced by frustrated total internal reflection and the properties of the evanescent wave (Lee and Poon, 2004). To generate the Fano resonance in an appropriately designed structure, an evanescent wave, an electromagnetic wave propagating in the near field across an interface between two media with different refractive indices, can be used. The ability of the evanescent wave to penetrate media with a higher refractive index allows the connection between the discrete resonance state and the continuum of scattering states and can result in the typical Fano resonance line shape. This study offers a first theoretical description of the Fano resonance phenomenon, an optical event that results from the interference between subwavelength excitonic nanoparticle and the scattering of evanescent waves. Using the angle-resolved prism-coupling method, we aim to unravel the details of this phenomenon and elucidate the fundamental mechanisms guiding the interaction between nanoparticles and evanescent waves. This approach is an important tool to show the correlation between the critical angle required for the formation of evanescent waves and the Fano resonance. Furthermore, the correlation between the Fano resonance and the size of the excitonic nanoparticles and the oscillator power, an important parameter in Frenkel excitons, is investigated.

The simulations in this paper were performed using Lumerical FDTD software.

We used the Lorentz model (Oughstun and Cartwright, 2003) to characterize nanoparticles with excitonic resonance. A nanoparticle with an excitonic resonance at 2.11 eV and a linewidth of 32 meV was identified for use in simulations. It also has a background permittivity of 2.04. In the simulation, we first build an infinite SiO2 model according to nanoparticles, on which excitonic nanocrystal is placed. We used a frequency domain and power monitor with a plane wave source and 10000 nm FDTD x-span workspace and perfectly matched layer (PML) boundary conditions are used. Firstly, a simulation was performed with a nanoparticle placed on a prism without excitonic properties. This resulted in the generation of a broadband background spectrum due to the evanescent wave. First, a simulation was performed with a nanoparticle placed on a prism without excitonic properties. This resulted in the generation of a broadband background spectrum facilitated by the evanescent wave. A second simulation was then performed, this time incorporating the previously mentioned excitonic properties into the nanoparticle. The result of this second simulation was then subtracted from the background to produce the results presented in this work.

Fano resonance systems have two states: open channel or continuum state and closed channel or discrete state. The closed channel is responsible for resonance, while the open channel is associated with scattering. The ephemeral interplay within the channel, embodied by an operator, is represented by $\hat{U}(t_1, t_2)$. The explanation of the Fano resonance is possible through the application of the S-matrix, also known as the scattering matrix, within the framework of quantum field theory. The components of the scattering matrix are denoted as ψ_{sc} for continuum state and ψ_{dc} for discrete state.

$$\mathbf{S} = \left\langle \psi_{dc} \left| \hat{U}(\infty, -\infty) \right| \psi_{sc} \right\rangle \tag{3.1}$$

For one open channel, the cross section is (Connerade and Lane, 1988),

$$\sigma(E) = \frac{4K^2}{1 + K^2}. \tag{3.2}$$

Where $K = tan(\omega_0 + \delta_0)$. The resonance frequency, denoted as ω_0 , is associated with the absorption process, while δ_0 represents the phase shift that results from the scattering process.

$$tan(\omega_0) = \frac{\Gamma}{2(E - E_0)}, \tag{3.3}$$

where Γ is the line width of the resonance, and E is the energy of the resonance. Therefore,

$$K = \frac{(E - E_0)\, tan(\delta) + \frac{1}{2}\Gamma}{(E - E_0) - \frac{1}{2}\Gamma tan(\delta)}. \tag{3.4}$$

According to these results, if we rewrite the cross section,

$$\sigma\,(E) = \frac{4K^2}{1 + K^2} = 4sin^2\delta \frac{\left[(E - E_0) + \frac{1}{2}\Gamma cot(\delta)\right]^2}{(E - E_0)^2 + \left(\frac{1}{2}\Gamma\right)^2}. \tag{3.5}$$

The standard Fano formula is

$$\sigma\,(E) = D^2 \frac{(q + \Omega)^2}{1 + \Omega^2} \tag{3.6}$$

where Fano parameter $q = cot\delta$, $D^2 = 4sin^2\delta$ and $\Omega = 2\,(E - E_0)\,/\Gamma$. An alternative approach to Fano resonance characterization is to use two coupled driven oscillator model (Joe et al., 2006), (Limonov et al., 2017), (Khanikaev et al., 2013). The matrix equation of the model is

$$\begin{pmatrix} \omega_1 - \omega - i\,\gamma_1 & g \\ g & \omega_2 - \omega - i\gamma_2 \end{pmatrix} \begin{pmatrix} x_1 \\ x_2 \end{pmatrix} = i \begin{pmatrix} f_1 \\ f_2 \end{pmatrix}, \tag{3.7}$$

where g is coupling constant, x_1 and x_2 are the amplitudes of the oscillators, ω_1 and ω_2 are the resonance frequencies of the oscillators, γ_1 and γ_2 are the damping coefficients, and f_1 and f_2 are the external forces defined by the driving frequency ω ($f_1 \neq 0, f_2 = 0$). Within the framework of the Fano resonance, a scenario with coupled resonances in the weak coupling regime can be constructed. One of the oscillators is described as an open channel with a broadband continuum state and a significant damping coefficient, denoted by γ_1, while the other oscillator is described as a closed channel with a discrete state, characterized by γ_2. It is also important that the coupling strength, denoted g satisfies the condition $\gamma_1 \gg g \gg \gamma_2$ (Limonov, 2021). The Fano resonance spectrum can be calculated

from the square of the x_1 amplitude:

$$|x_1(\Omega)|^2 \approx \left|f_1^2\right| \frac{\gamma_1^2}{(\omega_1-\omega_2)^2+\gamma_1^2} \frac{(\Omega+q)^2}{\left(\Omega^2+1\right)}. \tag{3.8}$$

We employ the angle-resolved prism-coupling technique to generate evanescent wave scattering to study the Fano resonance generated by the interference between evanescent wave scattering and absorption of excitonic nanoparticles located on the prism surface at subwavelength dimensions. This method provides precise control over the propagation characteristics of the evanescent wave, allowing the systematic study of its interaction with different nanostructures. Coupling light to a prism at angles above the critical angle induces an evanescent wave that propagates along the prism-sample interface. The exponential decay of the evanescent wave in the sample allows the study of optical properties in near-surface region.

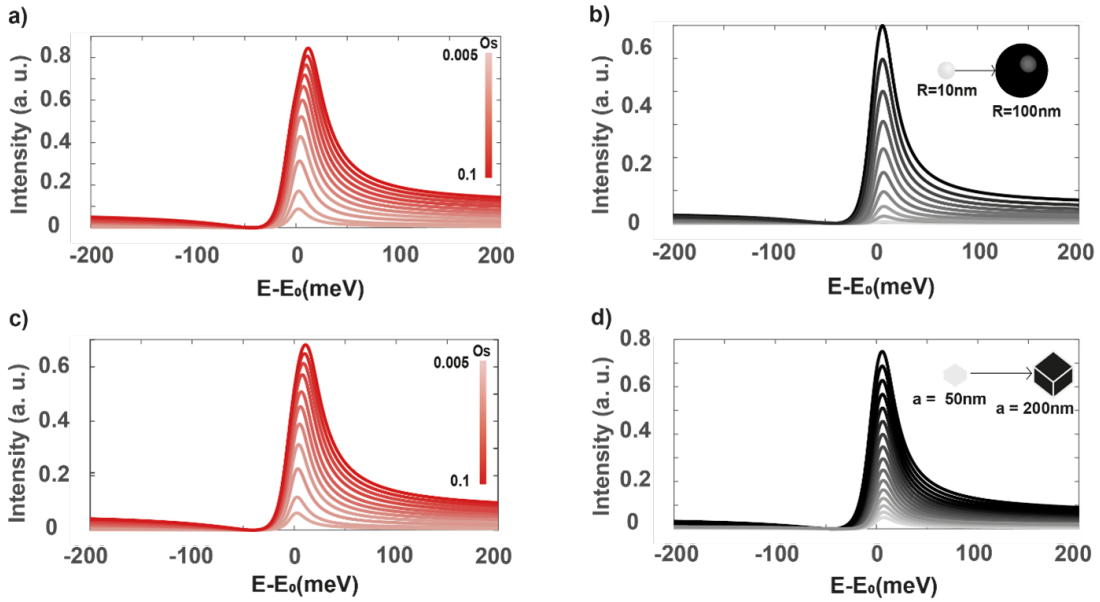

Figure 3.1. Influence of oscillation strength and excitonic nanoparticle size on Fano resonance In a) and b), the nanoparticle shape is a sphere and in c) and d), the shape is cube. In a) and c) the oscillation strength of the excitonic nanoparticle is varied from 0.005 to 0.1. This results in a change in the spectrum of the nanoparticle, with the peak shifting to a higher energy as the oscillation strength increases. In b) the radius of the sphere ranges from 10 to 100 nm, in d) the side length of the cube varies from 50 to 200 nm.

The Lorentz model (Oughstun and Cartwright, 2003) is employed within the

Finite-Difference Time-Domain (FDTD) simulation framework to elucidate the behavior of excitonic nanoparticles. Using the Lorentz model to characterize material optics, we designed excitonic nanoparticles in accordance with an excitonic dye, TDBC (J-aggregate) (Bellessa et al., 2004), to exhibit a specific relative permittivity. We successfully achieved the desired relative permittivity by intelligently varying the material properties in the Lorentz model. This methodology is demonstrated by fine-tuning the Lorentz permittivity (oscillator strength), a critical parameter in the Lorentz model, for excitonic particles with different nanostructures and revealing its effect on the Fano resonance, as shown in figure 3.1 (a) for spherical nanoparticle and figure 3.1 (c) for square nanoparticle. The increased red coloration in these figures indicates a corresponding increase in the oscillator strength associated with the excitonic nanoparticle under study. An increase in the Lorentz permittivity of an excitonic nanoparticle can lead to increased scattering in the medium, resulting in a spectral shift of the peak absorption of the nanoparticle toward higher energy levels (Kuznetsov et al., 2016), as seen in figure 3.1 (a,c). This phenomenon can be attributed to the enhanced interaction between the excitonic resonance of the nanoparticle and the incident electromagnetic field, effectively changing the optical properties of the nanoparticle at the Fano resonance. Nanoparticles, which are much smaller than the wavelength of incident light, interact with light primarily by scattering (Kuznetsov et al., 2016). In addition, evanescent wave scattering is caused by the interaction between electromagnetic waves and nanoparticles with sub-wavelength dimensions (Zhang et al., 2021). Figure 3.1 (b,d) show the effect of nanoparticle size and shape on the Fano resonance properties. The Fano resonance study was performed for spherical (b) and cubic (d) excitonic nanoparticles of different sizes within the evanescent wave penetration depth constraints with a constant oscillator power of 0.05. The observed increase in intensity can only be attributed to increased scattering.

The Fano resonance arises from the interference between two distinct channels: an open channel characterized by evanescent wave scattering and a closed channel associated with excitonic absorption in nanoparticles. The open channel manifests itself as a continuum with broad state characteristics, while the closed channel exhibits discrete and narrow state behavior. The open channel facilitates manipulation and provides a means to study the properties of the Fano resonance. However, such manipulation is not possible with a closed channel. In the case of the closed channel, the only adjustable parameter is the oscillator strength. However, changing this parameter does not affect the absorbance except to increase the intensity. The oscillator strength and the size of the exciton nanoparticle exert significant influences on the open channel. As shown in figure 3.2 (a) and (c), we present the fit of two selected individual data points from figure 3.1 (a) and (b) according to equation 6. In figure 3.2 (c), we adjust the oscillator strength to control the open channel of exciton nanoparticles. This adjustment leads to changes permittivity of nanoparticle in the wavelength of exciton near the absorption resonance, thereby altering the refractive index.

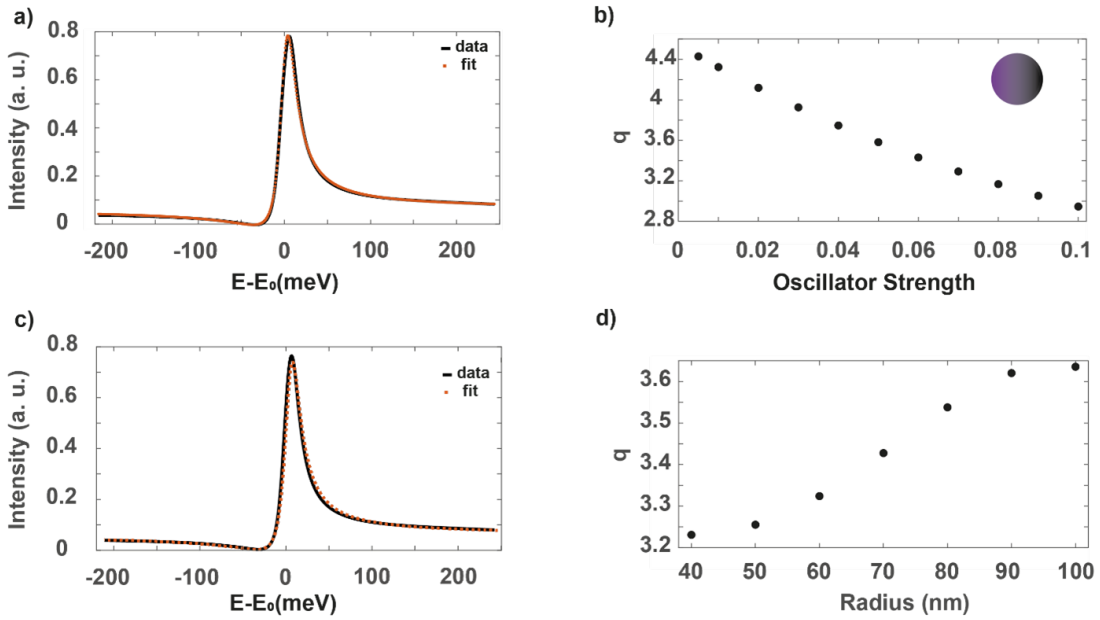

Figure 3.2. The effect of oscillation strength and sphere size on the Fano parameter (q). (a) Fit result for a single spectrum of a sphere with an oscillation strength of 0.1 and a radius of 50 nm. Black spectrum is simulation result and red dots are fit results. (b) Results of the Fano parameter for spherical nanoparticles based on the oscillation strength sweep. (c) A black line is observed when a sphere with a radius of 80 nm and an oscillation strength of 0.06 is examined with a single spectrum and red dots are fitting results of Fano formula. (d) The effect of the spherical nanoparticle radius in the range of 40 to 100 nm on the Fano parameter was investigated g from larger nanoparticles Kuznetsov et al. (2016), as no shift in the resonant frequency is observed.

Meanwhile, high-index dielectric structures can exploit optical resonances to manipulate light beyond the constraints imposed by free-space diffraction (Kuznetsov et al., 2016). The increasing disparity in the refractive indices between the nanoparticle and the prism surface leads to a pronounced increase in the phase shifts (δ) observed during volatile wave scattering. As a result, there is a decrease in the Fano parameter (q) associated with $q = cot\delta$ in phases below the $\pi/2$ phase, as shown in figure 3.2 (b). The Fano parameter's dependence on excitonic nanoparticle size is illustrated in figure 3.2 (d). Size-dependent tuning leads to a reduction in scattering as the particle size increases and approaches the excitation wavelength (Quality of scattering relation is $2\pi R/\lambda$) (Kuznetsov et al., 2016). The reduced evanescent scattering contributes to a phase shift and a reducing q value for phases below $\pi/2$, as shown in figure 3.2 (d).

Within the realm of light-matter interaction, the damping parameters governing the coupling between the two oscillators play a crucial role, as illustrated by equation 7. The variations in the absorption linewidth of the investigated excitonic nanoparticles have a significant influence on the Fano resonance. In the absence of a parameter that directly influences the scattering of the evanescent wave, it is also possible to study the influence of the Fano resonance on the subwavelength excitonic particles with different linewidths.

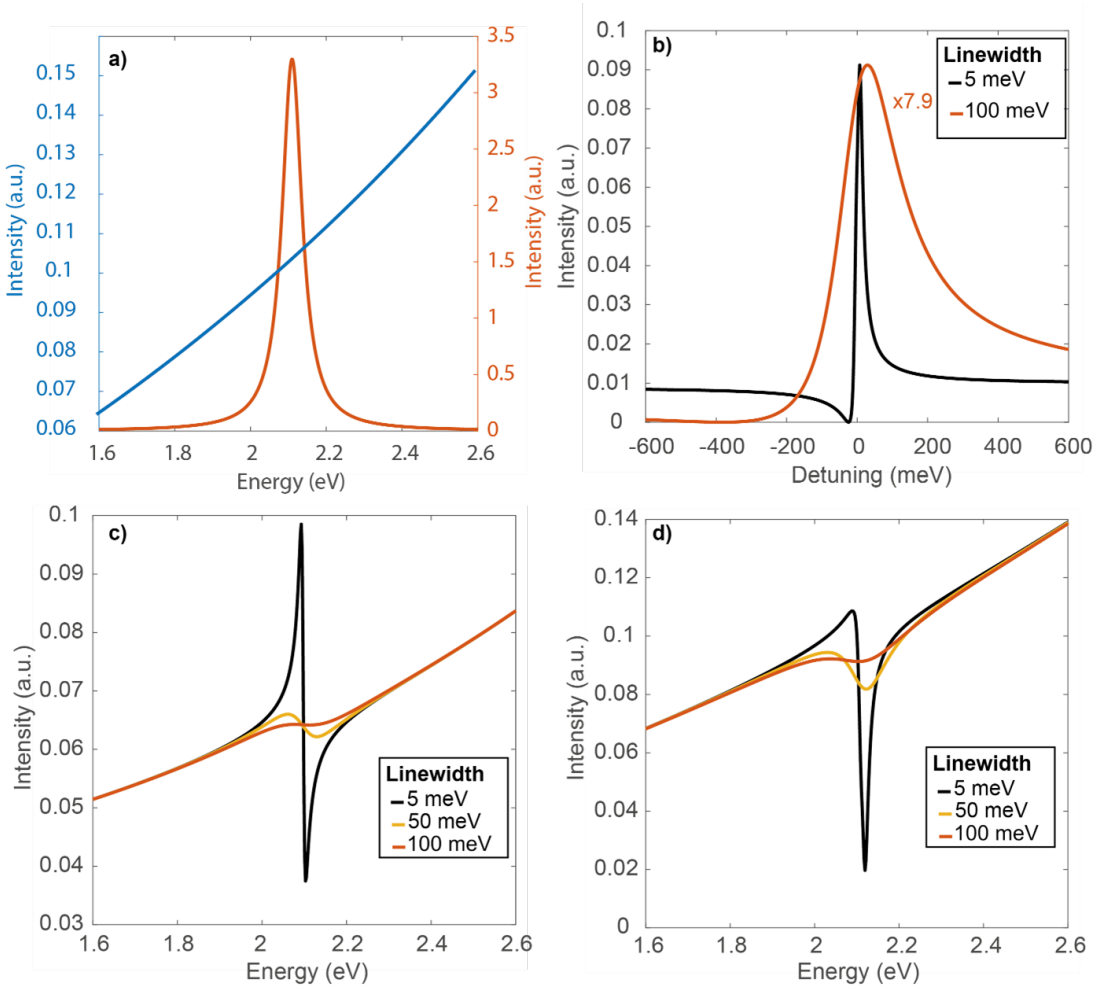

Figure 3.3. The Effect of Excitonic Absorption Linewidth on Fano Resonance. a) Red line is the absorption spectrum of the excitonic nanoparticle used in our simulations. Blue line is the broadband evanescent wave scattering spectrum for nanoparticles without excitonic properties on the prism. b) FDTD simulations were performed for excitonic nanoparticles on a prism configuration, with the linewidth of the black curve set to 5 meV and that of the red curve set to 100 meV and a 7.9-fold difference between their intensities was observed. c) Analytic results for different exciton absorbance linewidths. d) FDTD simulations result for different exciton absorbance linewidths in nanoparticles on a prism configuration.

Figure 3.3 (a) shows the spectral characteristics of a discrete state resulting from exciton absorption and a broadband continuum state resulting from a nanoparticle without excitonic properties (consistent with the zero Lorentz permittivity in Lorentz model (Oughstun and Cartwright, 2003)). In this work, optical simulations are performed with systematically varying parameters in a configuration created with an excitonic nanoparticle on a prism. As shown in figure 3.3 (b), the line width for the black curve is set at 5 meV, in contrast to the red curve, which is set at 100 meV. A remarkable observation from these simulations is the pronounced difference in their intensities, with the red curve having an intensity about 7.9 times that of the black curve. This can be attributed to the Lorentz model, which predicts an increase in intensity as the linewidth decreases. While this increase is

about 20 times in the exciton absorption spectrum, the Fano resonance, a consequence of destructive interference (Miroshnichenko et al., 2010), moderates this increase to about 7.9 times figure 3.3 (c) illustrates the results of the analysis for different linewidths, using the results of the Fano spectrum as shown in Equation 8, which is derived from equation 7. In this analysis, the resonance peak of the excitons is set at 2.1 eV. Meanwhile, the evanescent scattering description defines a spectrum with a broad linewidth (~ 1eV) and a resonance at high energy (>5eV), in agreement with the spectrum calculated in the simulation. In particular, the coupling parameter (g) between the two oscillators is larger than the exciton damping parameter, as predicted by theory, but remains significantly smaller than the damping parameter of the spectrum defined for evanescent wave scattering (~ 300meV) (Limonov et al., 2017). The simulation results depicted in figure 3.3 (d) illustrate how varied damping parameters of an exciton can affect the spectrum of an excitonic nanoparticle placed on a prism. The nanoparticle has an oscillator strength of 0.1 and a radius of 100 nm. Despite the close resemblance between the analytical and simulation results shown in figure 3.3 (c) and (d), the analytical result of Fano resonance has a much more intense Fano dip at a linewidth of 5 meV compared to the simulation result. The discrepancy arises from the different operational definitions of the open channel used in the analytical evaluation, as discussed earlier. This divergence results from the lack of a comprehensive definition that encompasses complex phenomena such as scattering within the analytical framework.

The angle-resolved prism-coupling technique can be used to excite evanescent waves beyond the critical angle due to the refractive index contrast between the mediums. In figure 3.4, The excitonic nanosphere used in this study has a radius of 100 nm and an oscillator strength of 0.1. Figure 3.4 shows the angle-dependent transmission results obtained using an excitonic nanosphere coupled to a prism. The results of the transmission spectrum simulations, which span the range from 0 to 55 degrees, are methodically plotted at 5-degree intervals. The initial degrees show spectral profiles similar to the exciton absorption spectrum. However, beyond 40 degrees, the emergence of the Fano resonance becomes apparent. The critical angle at the air-SiO_2 interface is wavelength dependent and ranges from 40 to 45 degrees. When this critical angle is exceeded, evanescent wave scattering occurs at the prism surface, resulting in a Fano resonance that is enhanced to 60 degree the angle of incidence increases. In evanescent waves, the penetration depth (d_p) is expressed by the formula (Griffiths, 1983):

$$d_p = \frac{\lambda}{2\pi n_1 \sqrt{sin^2\theta - (n_1/n_2)^2}}, \tag{3.9}$$

where λ is source wavelength, θ is incidence angle of source and $n_{1,2}$ are refractive index

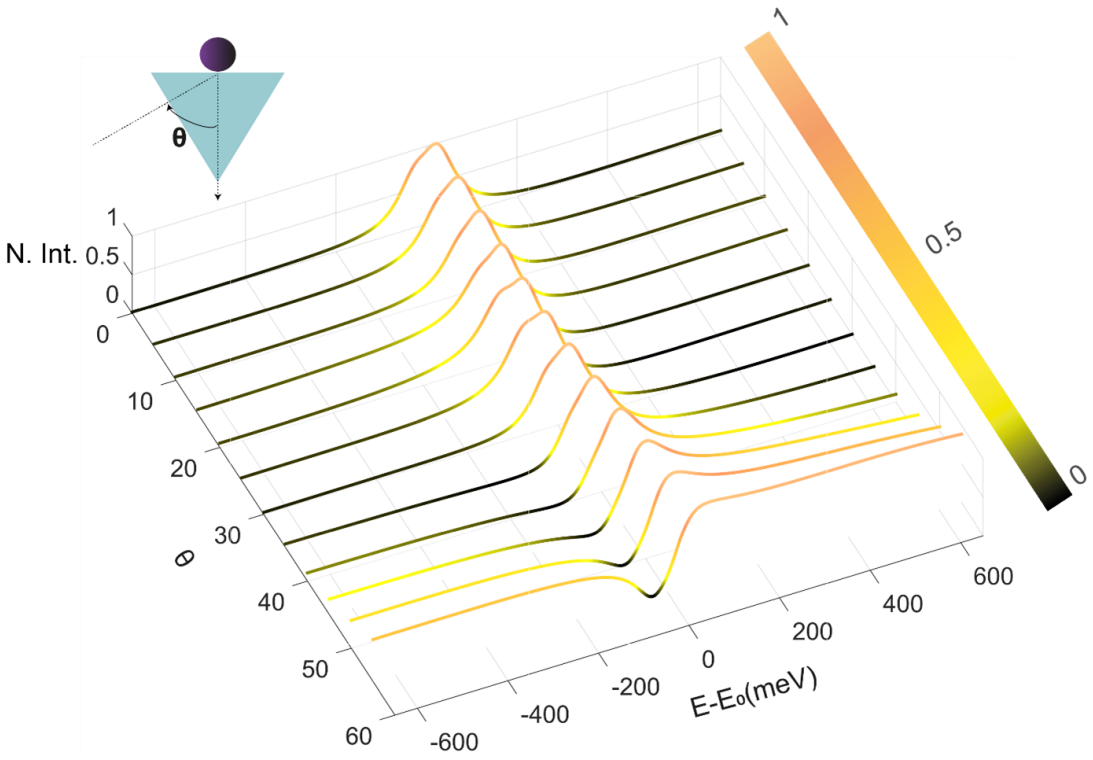

Figure 3.4. Radius sweep in the Kretschmann-Raether configuration. The simulation results of transmission spectra are displayed individually in 5-degree increments from 0 to 55 degrees. The Fano dip becomes noticeable after 40 degrees.

of mediums. This relationship implies that the intensity of evanescent wave scattering diminishes as the penetration depth decreases with increasing angle. This relationship implies that the decrease in evanescent wave penetration depth with increasing angle leads to a corresponding decrease in evanescent wave scattering intensity. Consequently, as the scattering intensity decreases, the Fano dip decreases.

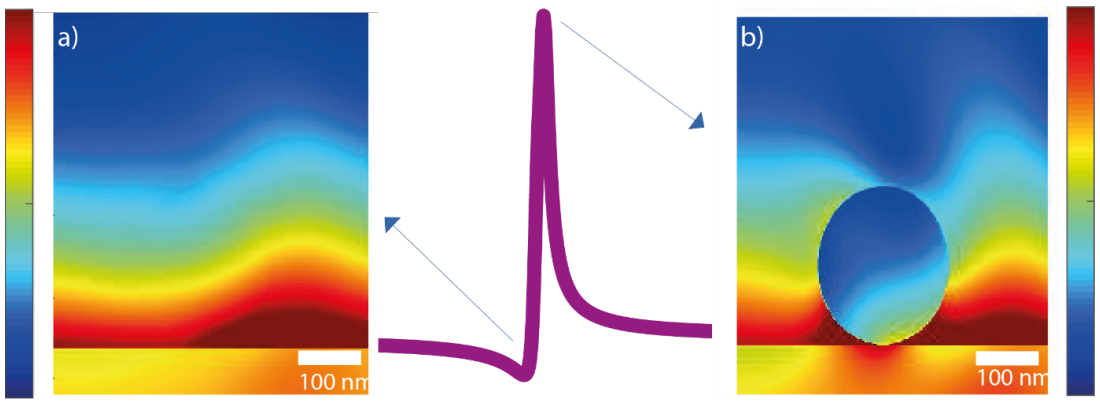

Figure 3.5. Spatial distribution of the electromagnetic field at the peak and dip of the Fano resonance a) The electric field distribution at the Fano dip point of the excitonic nanospheres with a radius of 100 nm on the prism is shown. b) The electric field distribution for the same nanoparticle at the peak of the Fano resonance is shown.

In figure 3.5, the spatial distribution of the electromagnetic field at the dip (a) and peak (b) of the Fano resonance for excitonic nanoparticles with an oscillator strength of 0.1, a radius of 100 nm, and an angle of incidence of 50 degrees. As shown in figure 3.5 (a), the excitonic nanoparticle located at the base of the Fano resonance prism exhibits electromagnetically induced transparency (EIT) like behavior within the electric field distribution. EIT can be conceptualized as a Fano resonance occurring at the same oscillator resonance ($\omega_1 = \omega_2$) (Limonov et al., 2017). Therefore, the dips of the Fano resonance are also expected to show remarkable transparency, as in figure 3.5 (a). The Fano resonance is manifested by the peak observed in the electric field distribution shown in figure 3.5 (b).

3.2 Conclusion

In summary, we have demonstrated for the first time the interference between the absorption of a subwavelength excitonic particle and the evanescent wave scattering facilitated by a prism, resulting in the formation of a Fano resonance. In this model, the discrete state is represented by the absorption of exciton nanoparticles, while the continuum state is characterized by evanescent wave scattering. We have shown that the system exhibits a direct correlation with the evanescent wave due to the scattering induced by the interaction between the evanescent wave - which can be generated beyond the critical angle by adjusting the angle of incident light in the system - and the subwavelength particles on the prism. We also conducted an analysis of the phase shifts that exhibit variations in relation to size and oscillator strength. The most important parameter for the generation of evanescent wave scattering is the subwavelength scale of the nanoparticles used (Roy et al., 2017), (Doicu et al., 2001). In the experimental setup, which is similar to the simulations performed in this study, the micron-order particles used begin to exhibit resonator-like behavior (Vasista and Barnes, 2020).

CHAPTER 4

Conclusion

This thesis investigates the light-matter interaction in both the strong and weak coupling regimes and discusses the results obtained. In the strong coupling regime, the eigenstates that arise when surface plasmon polaritons (SPPs) interact with excitons (top and bottom polaritons) are studied in detail. In particular, this work pioneers the use of hyperspectral imaging to unlock the secrets of exciton-polariton behavior in optical microcavities. This breakthrough enables hyperspectral imaging to visualize and spatially map these elusive quasiparticles, providing insights into their dynamics as well as a simple and effective method to study exciton-polaritons in optical microcavities.

Beyond strong coupling, the work moves into the realm of weak coupling, focusing on the Fano resonance. This unique phototonic phenomenon results from destructive interference between two optical paths, one discrete and narrow, the other broad and continuous. The research explores the losses governing the Fano resonance by studying the complex interaction between subwavelength excitonic nanoparticles placed on the surface of a prism and evanescent wave scattering. By rigorously analyzing the influence of parameters such as the angle of incidence of light, nanoparticle size, and absorption linewidth, the effects of such optical property variations on the Fano parameter (q) are investigated. The existence of such effects is theoretically demonstrated for the first time at the Fano resonance due to interference between subwavelength sized exciton nanoparticles and the evanescent wave.

REFERENCES

Agranovich, V. M., M. Litinskaia, and D. G. Lidzey (2003). Cavity polaritons in microcavities containing disordered organic semiconductors. *Physical Review B 67*(8), 085311.

Archambault, A., T. V. Teperik, F. Marquier, and J.-J. Greffet (2009). Surface plasmon fourier optics. *Physical Review B 79*(19), 195414.

Aslan, K., M. Wu, J. R. Lakowicz, and C. D. Geddes (2007). Fluorescent core- shell ag@ sio2 nanocomposites for metal-enhanced fluorescence and single nanoparticle sensing platforms. *Journal of the American Chemical Society 129*(6), 1524–1525.

Balci, F. M., S. Sarisozen, N. Polat, and S. Balci (2019). Colloidal nanodisk shaped plexcitonic nanoparticles with large rabi splitting energies. *The Journal of Physical Chemistry C 123*(43), 26571–26576.

Balci, F. M., S. Sarisozen, N. Polat, C. M. Guvenc, U. Karadeniz, A. Tertemiz, and S. Balci (2021). Laser assisted synthesis of anisotropic metal nanocrystals and strong light-matter coupling in decahedral bimetallic nanocrystals. *Nanoscale Advances 3*(6), 1674–1681.

Balci, S., E. Karademir, and C. Kocabas (2015). Strong coupling between localized and propagating plasmon polaritons. *Optics letters 40*(13), 3177–3180.

Balci, S., C. Kocabas, S. Ates, E. Karademir, O. Salihoglu, and A. Aydinli (2012). Tuning surface plasmon-exciton coupling via thickness dependent plasmon damping. *Physical Review B 86*(23), 235402.

Balili, R., V. Hartwell, D. Snoke, L. Pfeiffer, and K. West (2007). Bose-einstein condensation of microcavity polaritons in a trap. *Science 316*(5827), 1007–1010.

Baranov, D. G., M. Wersall, J. Cuadra, T. J. Antosiewicz, and T. Shegai (2018). Novel nanostructures and materials for strong light–matter interactions. *Acs Photonics 5*(1), 24–42.

Bek, A., R. Jansen, M. Ringler, S. Mayilo, T. A. Klar, and J. Feldmann (2008). Fluorescence enhancement in hot spots of afm-designed gold nanoparticle sandwiches. *Nano Letters 8*(2), 485–490.

Bellessa, J., C. Bonnand, J. Plenet, and J. Mugnier (2004). Strong coupling between surface plasmons and excitons in an organic semiconductor. *Physical review letters 93*(3), 036404.

Boller, K.-J., A. Imamoğlu, and S. E. Harris (1991). Observation of electromagnetically induced transparency. *Physical Review Letters 66*(20), 2593.

Borrmann, G. (1950). Die absorption von röntgenstrahlen im fall der interferenz. *Zeitschrift für Physik 127*(4), 297–323.

Byrnes, T., N. Y. Kim, and Y. Yamamoto (2014). Exciton–polariton condensates. *Nature Physics 10*(11), 803–813.

Cai, D.-J., Y.-H. Huang, W.-J. Wang, W.-B. Ji, J.-D. Chen, Z.-H. Chen, and S.-D. Liu (2015). Fano resonances generated in a single dielectric homogeneous nanoparticle with high structural symmetry. *The Journal of Physical Chemistry C 119*(8), 4252–4260.

Chikkaraddy, R., B. De Nijs, F. Benz, S. J. Barrow, O. A. Scherman, E. Rosta, A. Demetriadou, P. Fox, O. Hess, and J. J. Baumberg (2016). Single-molecule strong coupling at room temperature in plasmonic nanocavities. *Nature 535*(7610), 127–130.

Christensen, N. E. and B. Seraphin (1971). Relativistic band calculation and the optical properties of gold. *Physical Review B 4*(10), 3321.

Christopoulos, S., G. B. H. Von Högersthal, A. Grundy, P. Lagoudakis, A. Kavokin, J. Baumberg, G. Christmann, R. Butté, E. Feltin, J.-F. Carlin, et al. (2007). Room-temperature polariton lasing in semiconductor microcavities. *Physical review letters 98*(12), 126405.

Connerade, J.-P. and A. Lane (1988). Interacting resonances in atomic spectroscopy. *Reports on Progress in Physics 51*(11), 1439.

Doicu, A., Y. Eremin, and T. Wriedt (2001). Scattering of evanescent waves by a particle on or near a plane surface. *Computer physics communications 134*(1), 1–10.

Ergoktas, M. S., S. Soleymani, N. Kakenov, K. Wang, T. B. Smith, G. Bakan, S. Balci, A. Principi, K. S. Novoselov, S. K. Ozdemir, et al. (2022). Topological engineering of terahertz light using electrically tunable exceptional point singularities. *Science 376*(6589), 184–188.

Fan, P., Z. Yu, S. Fan, and M. L. Brongersma (2014). Optical fano resonance of an individual semiconductor nanostructure. *Nature materials 13*(5), 471–475.

Fano, U. (1961). Effects of configuration interaction on intensities and phase shifts. *Physical review 124*(6), 1866.

Faraji-Dana, M., E. Arbabi, H. Kwon, S. M. Kamali, A. Arbabi, J. G. Bartholomew, and A. Faraon (2019). Hyperspectral imager with folded metasurface optics. *ACS Photonics 6*(8), 2161–2167.

Finkelstein-Shapiro, D., P.-A. Mante, S. Sarisozen, L. Wittenbecher, I. Minda, S. Balci, T. Pullerits, and D. Zigmantas (2021). Understanding radiative transitions and relaxation pathways in plexcitons. *Chem 7*(4), 1092–1107.

Frenkel, J. (1931). On the transformation of light into heat in solids. i. *Physical Review 37*(1), 17.

Gebhardt, C., M. Förg, H. Yamaguchi, I. Bilgin, A. D. Mohite, C. Gies, M. Florian, M. Hartmann, T. W. Hänsch, A. Högele, et al. (2019). Polariton hyperspectral imaging of two-dimensional semiconductor crystals. *Scientific reports 9*(1), 13756.

Gibbs, H., G. Khitrova, and S. Koch (2011). Exciton–polariton light–semiconductor coupling effects. *Nature Photonics 5*(5), 273–273.

Goetz, A. F., G. Vane, J. E. Solomon, and B. N. Rock (1985). Imaging spectrometry for earth remote sensing. *science 228*(4704), 1147–1153.

Grésillon, S., L. Aigouy, A. Boccara, J. Rivoal, X. Quelin, C. Desmarest, P. Gadenne, V. Shubin, A. Sarychev, and V. M. Shalaev (1999). Experimental observation of localized optical excitations in random metal-dielectric films. *Physical Review Letters 82*(22), 4520.

Griffiths, P. R. (1983). Fourier transform infrared spectrometry. *Science 222*(4621), 297–302.

Guvenc, C. M., F. M. Balci, S. Sarisozen, N. Polat, and S. Balci (2020). Colloidal bimetallic nanorings for strong plasmon exciton coupling. *The Journal of Physical Chemistry C 124*(15), 8334–8340.

Guvenc, C. M., N. Polat, and S. Balci (2020). Strong plasmon–exciton coupling in colloidal halide perovskite nanocrystals near a metal film. *Journal of Materials Chemistry C 8*(46), 16520–16526.

Hecht, E. (2012). *Optics*. Pearson Education India.

Indhu, A., L. Keerthana, and G. Dharmalingam (2023). Plasmonic nanotechnology for photothermal applications–an evaluation. *Beilstein Journal of Nanotechnology 14*(1), 380–419.

Jaynes, E. T. and F. W. Cummings (1963). Comparison of quantum and semiclassical radiation theories with application to the beam maser. *Proceedings of the IEEE 51*(1), 89–109.

Joe, Y. S., A. M. Satanin, and C. S. Kim (2006). Classical analogy of fano resonances. *Physica Scripta 74*(2), 259.

Junginger, A., F. Wackenhut, A. Stuhl, F. Blendinger, M. Brecht, and A. J. Meixner (2020). Tunable strong coupling of two adjacent optical $\lambda/2$ fabry-pérot microresonators. *Optics Express 28*(1), 485–493.

Kéna-Cohen, S., M. Davanço, and S. Forrest (2008). Strong exciton-photon coupling in an organic single crystal microcavity. *Physical review letters 101*(11), 116401.

Kéna-Cohen, S. and S. Forrest (2010). Room-temperature polariton lasing in an organic single-crystal microcavity. *Nature Photonics 4*(6), 371–375.

Kéna-Cohen, S., S. A. Maier, and D. D. Bradley (2013). Ultrastrongly coupled exciton–polaritons in metal-clad organic semiconductor microcavities. *Advanced Optical Materials 1*(11), 827–833.

Kerker, M., D.-S. Wang, and C. Giles (1983). Electromagnetic scattering by magnetic spheres. *JOSA 73*(6), 765–767.

Khanikaev, A. B., C. Wu, and G. Shvets (2013). Fano-resonant metamaterials and their applications. *Nanophotonics 2*(4), 247–264.

Khitrova, G., H. Gibbs, M. Kira, S. W. Koch, and A. Scherer (2006). Vacuum rabi splitting in semiconductors. *Nature physics 2*(2), 81–90.

Kittel, C. (2005). *Introduction to solid state physics*. John Wiley & sons, inc.

Klingshirn, C. F. (2012). *Semiconductor optics*. Springer Science & Business Media.

Kuznetsov, A. I., A. E. Miroshnichenko, M. L. Brongersma, Y. S. Kivshar, and B. Luk'yanchuk (2016). Optically resonant dielectric nanostructures. *Science 354*(6314), aag2472.

Lee, H.-T. and A. W. Poon (2004). Fano resonances in prism-coupled square micropillars. *Optics letters 29*(1), 5–7.

Lee, H.-T., L. Zhou, and A. W. Poon (2005). Fano resonances in prism-coupled multimode square micropillar resonators. *Optics letters 30*(12), 1527–1529.

Lei, F., B. Peng, Ş. K. Özdemir, G. L. Long, and L. Yang (2014). Dynamic fano-like resonances in erbium-doped whispering-gallery-mode microresonators. *Applied Physics Letters 105*(10).

Lerario, G., A. Fieramosca, F. Barachati, D. Ballarini, K. S. Daskalakis, L. Dominici, M. De Giorgi, S. A. Maier, G. Gigli, S. Kéna-Cohen, et al. (2017). Room-temperature superfluidity in a polariton condensate. *Nature Physics 13*(9), 837–841.

Liang, W. (1970). Excitons. *Physics Education 5*(4), 226.

Lidzey, D. G., D. Bradley, M. Skolnick, T. Virgili, S. Walker, and D. Whittaker (1998). Strong exciton–photon coupling in an organic semiconductor microcavity. *Nature 395*(6697), 53–55.

Lidzey, D. G., D. D. Bradley, A. Armitage, S. Walker, and M. S. Skolnick (2000). Photon-mediated hybridization of frenkel excitons in organic semiconductor microcavities. *Science 288*(5471), 1620–1623.

Limonov, M. F. (2021). Fano resonance for applications. *Advances in Optics and Photonics 13*(3), 703–771.

Limonov, M. F., M. V. Rybin, A. N. Poddubny, and Y. S. Kivshar (2017). Fano resonances in photonics. *Nature Photonics 11*(9), 543–554.

Liu, X., T. Galfsky, Z. Sun, F. Xia, E.-c. Lin, Y.-H. Lee, S. Kéna-Cohen, and V. M. Menon (2015). Strong light–matter coupling in two-dimensional atomic crystals. *Nature Photonics 9*(1), 30–34.

Markoš, P. (2015). Fano resonances and band structure of two-dimensional photonic structures. *Physical Review A 92*(4), 043814.

Miroshnichenko, A. E., S. Flach, and Y. S. Kivshar (2010). Fano resonances in nanoscale structures. *Reviews of Modern Physics 82*(3), 2257.

Miroshnichenko, A. E. and Y. S. Kivshar (2012). Fano resonances in all-dielectric oligomers. *Nano letters 12*(12), 6459–6463.

Mock, J. J., R. T. Hill, A. Degiron, S. Zauscher, A. Chilkoti, and D. R. Smith (2008). Distance-dependent plasmon resonant coupling between a gold nanoparticle and gold film. *Nano letters 8*(8), 2245–2252.

Moreau, A., C. Ciracì, J. J. Mock, R. T. Hill, Q. Wang, B. J. Wiley, A. Chilkoti, and D. R. Smith (2012). Controlled-reflectance surfaces with film-coupled colloidal nanoantennas. *Nature 492*(7427), 86–89.

Nosrati, S., T. Rammler, A. J. Meixner, and F. Wackenhut (2021). Combining optical strong mode coupling with polaritonic coupling in a $\lambda/2$ fabry–perot microresonator. *The Journal of Physical Chemistry C 125*(23), 13024–13032.

Nozaki, K., A. Shinya, S. Matsuo, T. Sato, E. Kuramochi, and M. Notomi (2013). Ultralow-energy and high-contrast all-optical switch involving fano resonance based on coupled photonic crystal nanocavities. *Optics express 21*(10), 11877–11888.

Oughstun, K. E. and N. A. Cartwright (2003). On the lorentz-lorenz formula and the lorentz model of dielectric dispersion. *Optics express 11*(13), 1541–1546.

Ozbay, E. (2006). Plasmonics: merging photonics and electronics at nanoscale dimensions. *science 311*(5758), 189–193.

Ozceri, E., N. Polat, S. Balci, and E. Tarhan (2021). Room temperature emission from single defects in wo3 enhanced by plasmonic nanocrystals. *Applied Physics Letters 118*(23).

Pala, R. A., J. White, E. Barnard, J. Liu, and M. L. Brongersma (2009). Design of plasmonic thin-film solar cells with broadband absorption enhancements. *Advanced materials 21*(34), 3504–3509.

Raether, H. (2006). Surface plasmons on gratings. *Surface plasmons on smooth and rough surfaces and on gratings*, 91–116.

Rahmani, M., B. Luk'yanchuk, and M. Hong (2013). Fano resonance in novel plasmonic nanostructures. *Laser & Photonics Reviews 7*(3), 329–349.

Ribeiro, R. F., L. A. Martínez-Martínez, M. Du, J. Campos-Gonzalez-Angulo, and J. Yuen-Zhou (2018). Polariton chemistry: controlling molecular dynamics with optical cavities. *Chemical science 9*(30), 6325–6339.

Rodriguez, S., A. Amo, I. Sagnes, L. Le Gratiet, E. Galopin, A. Lemaître, and J. Bloch (2016). Interaction-induced hopping phase in driven-dissipative coupled photonic microcavities. *Nature communications 7*(1), 11887.

Rodriguez, S. R.-K. (2016). Classical and quantum distinctions between weak and strong coupling. *European Journal of Physics 37*(2), 025802.

Roy, S., S. Pereira, H. Urbach, X. Wei, and O. El Gawhary (2017). Exploiting evanescent-wave amplification for subwavelength low-contrast particle detection. *Physical Review A 96*(1), 013814.

Rybin, M. V., K. B. Samusev, I. S. Sinev, G. Semouchkin, E. Semouchkina, Y. S. Kivshar, and M. F. Limonov (2013). Mie scattering as a cascade of fano resonances. *Optics express 21*(24), 30107–30113.

Safiabadi Tali, S. A. and W. Zhou (2019). Multiresonant plasmonics with spatial mode overlap: overview and outlook. *Nanophotonics 8*(7), 1199–1225.

Sarisozen, S., N. Polat, F. Mert Balci, C. M. Guvenc, C. Kocabas, H. G. Yaglioglu, and S. Balci (2022). Strong coupling of carbon quantum dots in liquid crystals. *The Journal of Physical Chemistry Letters 13*(16), 3562–3570.

Sherry, L. J., R. Jin, C. A. Mirkin, G. C. Schatz, and R. P. Van Duyne (2006). Localized surface plasmon resonance spectroscopy of single silver triangular nanoprisms. *Nano letters 6*(9), 2060–2065.

Sun, Y., P. Wen, Y. Yoon, G. Liu, M. Steger, L. N. Pfeiffer, K. West, D. W. Snoke, and K. A. Nelson (2017). Bose-einstein condensation of long-lifetime polaritons in thermal equilibrium. *Physical review letters 118*(1), 016602.

Tavis, M. and F. W. Cummings (1968, Jun). Exact solution for an n-molecule—radiation-field hamiltonian. *Phys. Rev. 170*, 379–384.

Tischler, J. R., M. S. Bradley, Q. Zhang, T. Atay, A. Nurmikko, and V. Bulović (2007). Solid state cavity qed: Strong coupling in organic thin films. *Organic Electronics 8*(2-3), 94–113.

Vasa, P. and C. Lienau (2018). Strong light–matter interaction in quantum emitter/metal hybrid nanostructures. *Acs Photonics 5*(1), 2–23.

Vasista, A. B. and W. L. Barnes (2020). Molecular monolayer strong coupling in dielectric soft microcavities. *Nano Letters 20*(3), 1766–1773.

Wannier, G. H. (1937). The structure of electronic excitation levels in insulating crystals. *Physical Review 52*(3), 191.

Weidman, M. C., M. Seitz, S. D. Stranks, and W. A. Tisdale (2016). Highly tunable colloidal perovskite nanoplatelets through variable cation, metal, and halide composition. *ACS nano 10*(8), 7830–7839.

Weisbuch, C., M. Nishioka, A. Ishikawa, and Y. Arakawa (1992). Observation of the coupled exciton-photon mode splitting in a semiconductor quantum microcavity. *Physical review letters 69*(23), 3314.

Xia, Y., Y. Xiong, B. Lim, and S. E. Skrabalak (2009). Shape-controlled synthesis of metal nanocrystals: simple chemistry meets complex physics? *Angewandte Chemie International Edition 48*(1), 60–103.

Xu, H., E. J. Bjerneld, M. Käll, and L. Börjesson (1999). Spectroscopy of single hemoglobin molecules by surface enhanced raman scattering. *Physical review letters 83*(21), 4357.

Yang, H., D. Zhao, S. Chuwongin, J.-H. Seo, W. Yang, Y. Shuai, J. Berggren, M. Hammar, Z. Ma, and W. Zhou (2012). Transfer-printed stacked nanomembrane lasers on silicon. *Nature Photonics 6*(9), 615–620.

Ye, J., F. Wen, H. Sobhani, J. B. Lassiter, P. Van Dorpe, P. Nordlander, and N. J. Halas (2012). Plasmonic nanoclusters: near field properties of the fano resonance interrogated with sers. *Nano letters 12*(3), 1660–1667.

Yu, Y., W. Xue, E. Semenova, K. Yvind, and J. Mork (2017). Demonstration of a self-pulsing photonic crystal fano laser. *Nature Photonics 11*(2), 81–84.

Yuen-Zhou, J., S. K. Saikin, T. Zhu, M. C. Onbasli, C. A. Ross, V. Bulovic, and M. A. Baldo (2016). Plexciton dirac points and topological modes. *Nature Communications 7*(1), 11783.

Zengin, G., M. Wersäll, S. Nilsson, T. J. Antosiewicz, M. Käll, and T. Shegai (2015). Realizing strong light-matter interactions between single-nanoparticle plasmons and molecular excitons at ambient conditions. *Physical review letters 114*(15), 157401.

Zhang, H., Z. Chen, and X. Wu (2021). Scattering of evanescent wave generated by total reflection. *Journal of Quantitative Spectroscopy and Radiative Transfer 260*, 107480.

Zhang, J., X. Leroux, E. Durán-Valdeiglesias, C. Alonso-Ramos, D. Marris-Morini, L. Vivien, S. He, and E. Cassan (2018). Generating fano resonances in a single-waveguide silicon nanobeam cavity for efficient electro-optical modulation. *ACS photonics 5*(11), 4229–4237.

Zhang, S., K. Bao, N. J. Halas, H. Xu, and P. Nordlander (2011). Substrate-induced fano resonances of a plasmonic nanocube: a route to increased-sensitivity localized surface plasmon resonance sensors revealed. *Nano letters 11*(4), 1657–1663.

Zhang, W., A. O. Govorov, and G. W. Bryant (2006). Semiconductor-metal nanoparticle molecules: Hybrid excitons and the nonlinear fano effect. *Physical review letters 97*(14), 146804.

VITA

EDUCATION

2023, **PhD in Photonics Science and Engineering**,
Graduate School of Engineering and Sciences, İzmir Institute of Technology, İzmir/Turkey
Thesis Title: Strong and Weak Light-Matter Interaction in Plasmonics and Optical Cavities.
Supervisor: Prof. Dr. Sinan BALCI

2017, **Master of Science (M.Sc.) in Physics,**
Graduate School of Engineering and Sciences, İzmir Institute of Technology, İzmir/Turkey
Thesis Title: Temperature Dependence of Zero Phonon Line Emission from Defects in Hexagonal Boron Nitride and Design of Photon-Pair Source
Supervisor: Assoc. Prof. Dr. Serkan ATEŞ

2015, Bachelor of Science in Physics
Department of Physics, Faculty of Science, Ihsan Doğramacı Bilkent University, Ankara/Turkey

PUBLICATIONS

1. Nahit Polat , Ozan Yakar, Sahin K. Özdemir, and Sinan Balci. Hyperspectral Imaging of Exciton Polaritons in Optical Microcavities. (In Review at *ACS Photonics*)
2. Nahit Polat, Sahin K. Özdemir, and Sinan Balci. Fano Resonance by Evanescent Wave. (to be submitted)
3. Sarisozen, S., Polat, N., Mert Balci, F., Guvenc, C. M., Kocabas, C., Yaglioglu, H. G., & Balci, S. (2022). Strong coupling of carbon quantum dots in liquid crystals. *The Journal of Physical Chemistry Letters*, *13*(16), 3562-3570.

4. Sarisozen, S., Tertemiz, N. A., Arica, T. A., Polat, N., Kocabas, C., Balci, F. M., & Balci, S. (2021). Transition Metal Salt Promoted, Green, and High-Yield Synthesis of Silver Nanowires for Flexible Transparent Conductive Electrodes. *ChemistrySelect*, *6*(44), 12548-12554.
5. Ozceri, E., Polat, N., Balci, S., & Tarhan, E. (2021). Room temperature emission from single defects in WO3 enhanced by plasmonic nanocrystals. *Applied Physics Letters*, *118*(23).
6. Balci, F. M., Sarisozen, S., Polat, N., Guvenc, C. M., Karadeniz, U., Tertemiz, A., & Balci, S. (2021). Laser assisted synthesis of anisotropic metal nanocrystals and strong light-matter coupling in decahedral bimetallic nanocrystals. *Nanoscale Advances*, *3*(6), 1674-1681.
7. Guvenc, C. M., Polat, N., & Balci, S. (2020). Strong plasmon–exciton coupling in colloidal halide perovskite nanocrystals near a metal film. *Journal of Materials Chemistry C*, *8*(46), 16520-16526.
8. Guvenc, C. M., Balci, F. M., Sarisozen, S., Polat, N., & Balci, S. (2020). Colloidal bimetallic nanorings for strong plasmon exciton coupling. *The Journal of Physical Chemistry C*, *124*(15), 8334-8340.
9. Yakar, O., Balci, O., Uzlu, B., Polat, N., Ari, O., Tunc, I., ... & Balci, S. (2019). Hybrid J-Aggregate–Graphene Phototransistor. *ACS Applied Nano Materials*, *3*(1), 409-417.
10. Balci, F. M., Sarisozen, S., Polat, N., & Balci, S. (2019). Colloidal nanodisk shaped plexcitonic nanoparticles with large Rabi splitting energies. *The Journal of Physical Chemistry C*, *123*(43), 26571-26576.
11. Uulu, D. A., Ashirov, T., Polat, N., Yakar, O., Balci, S., & Kocabas, C. (2019). Fourier transform plasmon resonance spectrometer using nanoslit-nanowire pair. *Applied Physics Letters*, *114*(25).

SCHOLARSHIPS

2018-2022 YÖK 100/2000 Ph.D. Scholarship.